

# Meridional Rossby Wave Generation and Propagation in the Maintenance of the Wintertime Tropospheric Double Jet

AMANDA K. O'ROURKE

*University of Michigan, Ann Arbor, Michigan*

GEOFFREY K. VALLIS

*University of Exeter, Devon, United Kingdom*

(Manuscript received 13 July 2015, in final form 15 February 2016)

## ABSTRACT

The eddy-driven and subtropical jets are two dynamically distinct features of the midlatitude upper-troposphere circulation that are often merged into a single zonal wind maximum. Nonetheless, the potential for a distinct double-jet state in the atmosphere exists, particularly in the winter hemisphere, and presents a unique zonal-mean flow with two waveguides and an interjet region with a weakened potential vorticity gradient upon which Rossby waves may be generated, propagate, reflect, and break.

The authors investigate the interaction of two groups of atmospheric waves—those with wavelengths longer and shorter than the deformation radius—within a double-jet mean flow in an idealized atmospheric model. Patterns of eddy momentum flux convergence for long and short waves differ greatly. Short waves behave following classic baroclinic instability theory such that their eddy momentum flux convergence is centered at the eddy-driven jet core. Long waves, on the other hand, reveal strong eddy momentum flux convergence along the poleward flank of the eddy-driven jet and within the interjet region. This pattern is enhanced when two jets are present in the zonal-mean zonal wind.

## 1. Introduction

The identification of the subtropical and eddy-driven jets as two related, but separate and distinct, features of the midlatitude atmosphere has received increasing research attention over the past decade (Lee and Kim 2003; Kim and Lee 2004; Vallis 2006). The classical approach to the general circulation of the midlatitude atmosphere is to describe the movement of a single “jet stream” corresponding to the single maximum in zonal-mean zonal wind. However, this single-jet-stream perspective muddles the strong underlying dynamics of two dynamically distinct jets. The interaction of these jets may have important implications for midlatitude dynamics, including low-frequency variability (Gerber and Vallis 2007; Vallis and Gerber 2008; Woollings et al. 2010; Barnes and Hartmann 2011) and long-term trends

of the midlatitude climate (Polvani and Kushner 2002; Kushner and Polvani 2004; Archer and Caldeira 2008). Here, we step back and consider the maintenance of meridionally separate, but interdependent, eddy-driven and subtropical jets from the perspective of the generation, propagation, and breaking of atmospheric waves.

Observations of an upper-tropospheric splitting of the zonal-mean zonal wind into an eddy-driven and subtropical jet occur in both the Northern Hemisphere (Bordi et al. 2007) and the Southern Hemisphere (Williams et al. 2007) winters. In the zonally asymmetric climatology, splitting of the subtropical and eddy-driven jets occurs often in regions such as the North Atlantic, where it has been related to the positive phase of the annular mode (Vallis and Gerber 2008). In the Southern Hemisphere, the regional separation of the jets between the South Pacific and eastern Australia during austral winter is referred to as the “Southern Hemisphere split jet” (Bals-Elsholz et al. 2001).

The appearance of a midlatitude double jet is often associated with the wintertime hemisphere where both strong seasonality and the development of a stratospheric

---

*Corresponding author address:* Amanda O'Rourke, University of Michigan, Room 2534, C.C. Little Building, 110 N. University Ave., Ann Arbor, MI 48109-1005.  
E-mail: amandao@princeton.edu

polar night jet play significant roles in the generation and propagation of atmospheric Rossby waves. Tropospheric baroclinicity grows in winter because of increasing meridional temperature gradients, increasing the strength of the eddy-driven jet in wintertime. The wintertime eddy generation region, along with the eddy-driven jet, have also been shown to be strongly dependent on the strength of the stratospheric polar vortex (Kushner and Polvani 2004; Bordi et al. 2007). Additionally, these two features of the wintertime hemisphere have been shown to influence the location of the subtropical and eddy-driven jets. The Hadley circulation shifts toward the summer hemisphere along with the subtropical jet at its boundary. Meanwhile, a strong stratospheric wintertime polar vortex is connected to a poleward shift of the latitude of surface westerlies and the eddy-driven jet (Polvani and Kushner 2002).

The separation and merger of the subtropical and eddy-driven jets have been found to be associated with the positive and negative phases of the annular modes, respectively (Gerber and Vallis 2009; Vallis et al. 2004; Monahan and Fyfe 2008; Eichelberger and Hartmann 2007). The annular modes describe the shifting of mass between the polar and midlatitude regions and are the dominant mode of variability within either hemisphere. The trigger for a shift in phase and the maintenance of that phase, from say a single-jet state to a sustained double-jet state, is still an open question. A number of studies point to the role of Rossby waves in the maintenance of the double-jet atmosphere (Lee and Kim 2003; Kim and Lee 2004).

The mechanisms driving the tropospheric jets are tied closely to the generation, propagation, and breaking of eddies originating in the storm tracks. Wave–mean flow interaction originates in mathematical arguments in which waves interact nonlinearly to produce fluxes of momentum and heat that can accelerate or decelerate the mean flow.

The double jet provides a unique opportunity to address wave–mean flow interaction where there are two distinct mean-flow regimes. For instance, novel wave dynamics described as interjet disturbances (IJD) by Kim and Lee (2004) within the region between the eddy-driven and subtropical jet cores has been found to arise from mechanisms separate from standard baroclinic waves.

Previous work by O'Rourke and Vallis (2013, hereafter OV13) found that the interaction of the two jets on a barotropic  $\beta$  plane can be associated with a wave–mean flow interaction involving eddies generated in the baroclinic region and their wavelength-dependent propagation into the region of the subtropical jet. Long waves, defined as those with zonal wavenumbers 1–5, were found to contribute to a merger of the subtropical and eddy-driven

jets. Meanwhile, short waves, wavenumbers 6–10, were confined to the region of forcing by both turning and critical latitudes, thus leading to a sharpening of the eddy-driven jet and little interaction with the subtropical jet.

OV13 conjectured that the difference between long-wave and short-wave interaction with the jet system was the result of different instability mechanisms as well as constraints on meridional propagation. Short waves were directly forced by stirring of the vorticity field and produced a pattern of eddy-momentum flux convergence similar to that expected from baroclinic instability in the atmosphere. Long waves, on the other hand, had centers of eddy momentum flux convergence within the interjet region and on the jet flanks. Long-wave eddy momentum flux divergence occurred at the cores of both the subtropical and eddy-driven jets—a stark contrast to that of short waves. The location of long-wave generation corresponds to the region of strongest meridional shear in the mean zonal flow. The influence of long waves on the mean flow is to decelerate the jet core, accelerate the jet flanks, and thus widen and weaken the jets.

This paper is an expansion of the work of OV13 to an idealized stratified, spherical domain, which includes organically occurring baroclinic instability within the storm tracks. We specifically focus on the influence of long and short waves in the maintenance of the atmospheric double jet on the sphere. We ask the question to what extent do long- and short-wave eddy momentum fluxes differ in the midlatitude troposphere, and what role, if any, does reflection play in the confinement of short-wave eddy activity. Within a range of double-jet mean states, we investigate the extent to which long waves exhibit a characteristic pattern of long-wave eddy momentum flux convergence that acts to blend the two jets while short waves, restricted by reflecting regions between the two jets, enhance the eddy-driven jet.

The structure of this paper is as follows. Section 2 covers the dry, primitive equation spherical model and the suite of experimental parameters chosen to develop a number of double- and single-jet atmospheric states. Section 3 describes the linear theory for limits of Rossby wave propagation originally developed in OV13 and modified here for the sphere. These bounds on the zonal phase speed are then applied to the results of an idealized primitive equations model on the sphere in section 4. A composite analysis looking at the development and maintenance of a double-jet structure in a given integration is discussed in section 6. A summary of our conclusions and discussion on future work is given in section 7.

## 2. Model and experiments

We consider the effects of Rossby wave propagation on midlatitude jet dynamics using a modification of the Held–Suarez primitive equations model with an extended stratosphere following Polvani and Kushner (2002). The model used here is run at T42 resolution with 40 vertical layers. The model implements a sponge layer at the top of the atmosphere. Details of this sponge layer can be found in the appendix of Polvani and Kushner (2002). Analysis is performed over the last 9728 days, neglecting the first 1536 days of spinup. In addition to the increase in vertical model layers of the original Held–Suarez model, the model includes two major modifications to the basic state. These modifications are summarized by two parameters:  $\gamma$ , which controls the strength of the stratospheric polar vortex, and  $\varepsilon$ , which controls the seasonality.

### a. Stratospheric polar vortex strength $\gamma$

The strength of the stratospheric polar vortex is controlled through the equilibrium stratospheric temperature and lapse rate. As in Polvani and Kushner (2002), the equilibrium stratospheric temperature as a function of pressure and latitude is given by

$$T_{\text{eq}}^{\text{strat}}(p, \phi) = [1 - W(\phi)]T_{\text{US}}(p) + W(\phi)T_{\text{PV}}(p), \quad (1)$$

where  $T_{\text{US}}$  is the *U.S. Standard Atmosphere, 1979* (COESA 1979), and

$$T_{\text{PV}} = T_{\text{US}}(p_T) \left( \frac{p}{p_T} \right)^{-R\gamma/g} \quad (2)$$

is the equilibrium polar vortex temperature with constant lapse rate  $\gamma$ .

The weighting function  $W(\phi)$  is the same as that of (A2) in Polvani and Kushner (2002) and is given by

$$W(\phi) = \frac{1}{2} \left[ 1 - \frac{\tanh(\phi - \phi_0)}{\delta\phi} \right], \quad (3)$$

where the transition between a stratospheric temperature given by the *U.S. Standard Atmosphere, 1979* (COESA 1979)  $T_{\text{US}}(p)$  and one with a constant lapse rate given by  $\gamma$  is located at  $\phi_0 = 50^\circ$  and the width of the transition region is  $\delta\phi = 10^\circ$ . The parameter  $\gamma$  is presented throughout this paper in units of kelvins per kilometer. While  $\gamma$  is a lapse rate, we refer to it as the stratospheric polar vortex parameter, as this is the dynamical result of changing the stratospheric lapse rate and the phenomenon we are directly interested in.

The weighting function limits our perturbation of the stratospheric temperature to the Northern Hemisphere

only. We can then increase the stratospheric lapse rate of the Northern Hemisphere by adjusting  $\gamma$  such that a larger  $\gamma$  is associated with a stronger vertical temperature gradient between the tropopause, the location which is determined by the equilibrium relaxation temperature, and the uppermost levels of the model.

Additionally, the transition region as controlled by the weighting function  $W(\phi)$  in (3) leads to a horizontal temperature gradient along a given pressure surface. This horizontal temperature gradient, through the thermal wind relationship, leads to a strong jet in the stratosphere. This jet is similar to the subtropical jet in the troposphere as it is driven by a relaxation of the temperature and exists in the absence of eddies, unlike the eddy-driven jet. Therefore, increasing the vertical lapse rate  $\gamma$  leads to a stronger meridional temperature gradient along a constant pressure surface and, thus, a stronger stratospheric polar vortex.

As a larger  $\gamma$  is associated with a colder pool of air aloft over the North Pole in this model, we can view model regimes with large  $\gamma$  as more winterlike. In addition to a large  $\gamma$ , the wintertime circulation is also associated with a shift in the tropospheric equilibrium profile as controlled by  $\varepsilon$ .

### b. Seasonal asymmetry

Chan and Plumb (2009) modified the idealized model of Polvani and Kushner (2002) to include fixed seasonality by changing the surface equilibrium temperatures. Chan and Plumb (2009) add an asymmetric heating component to the equilibrium temperature profile given by

$$T_{\text{eq}}^{\text{trop}}(p, \phi) = \max \left[ T_T, (T_0 - \delta T) \left( \frac{p}{p_0} \right)^\kappa \right], \quad (4)$$

where

$$\delta T = \delta_y \sin^2(\phi) + \varepsilon \sin\phi + \delta_z \log(p/p_0) \cos^2\phi. \quad (5)$$

Here,  $\delta_y = 10$  K,  $\delta_z = 50$  K,  $p_0 = 1000$  hPa,  $T_0 = 315$  K, and  $T_T = 200$  K are constants. The additional heating term  $\varepsilon \sin\phi$  adds heat asymmetrically to one hemisphere or the other, depending on the sign of the seasonality parameter  $\varepsilon$ . We can then obtain a simulated Northern Hemisphere winter by increasing  $\varepsilon > 0$ .

We vary  $\varepsilon$  across four values ranging from no asymmetrical heating between the hemispheres (equinox conditions) for  $\varepsilon = 0$  K and a relatively strong Northern Hemispheric winter regime with  $\varepsilon = 30$  K. The location of maximum surface heating moves to the Southern Hemisphere with increasing  $\varepsilon$ , with the greatest distance off equator being at  $22^\circ$ S.

TABLE 1. Experiments taken from Chan and Plumb (2009) and associated parameters. Cases classified as having a double jet, or a well-separated subtropical and eddy-driven jet, in a statistically steady state are in boldface.

Expt	Seasonal asymmetry (K)	Vortex strength ( $\text{K km}^{-1}$ )
0a	0	1
0b	0	2
0c	0	3
0d	0	4
1a	10	1
1b	10	2
1c	10	3
1d	10	4
2a	20	1
2b	20	2
<b>2c</b>	<b>20</b>	<b>3</b>
<b>2d</b>	<b>20</b>	<b>4</b>
<b>3a</b>	<b>30</b>	<b>1</b>
<b>3b</b>	<b>30</b>	<b>2</b>
<b>3c</b>	<b>30</b>	<b>3</b>
<b>3d</b>	<b>30</b>	<b>4</b>

### c. Obtaining a double-jet basic state

Both the seasonal asymmetry  $\varepsilon$  and stratospheric jet strength  $\gamma$  parameters have a strong influence on the location and magnitude of the tropospheric jets (Polvani and Kushner 2002; Kushner and Polvani 2004; Chan and Plumb 2009). As such, we use these parameters as knobs to attain a wide variety of single- and double-jet states following the mindset of OV13. In OV13, the locations of the eddy-driven and subtropical jets were controlled directly through the location of a zonally symmetric wavemaker and Newtonian relaxation to a basic state.

We are using these parameters  $\varepsilon$  and  $\gamma$  strictly to obtain a clean series of similar tropospheric jet conditions, to examine how eddies maintain a single- and double-jet state, and to explore how the conditions of the mean flow influence the propagation of eddies. It should be noted that we are not looking at the dynamical mechanisms as to how  $\varepsilon$  and  $\gamma$  adjust the tropospheric state. Further information on those topics can be found in Polvani and Kushner (2002), Kushner and Polvani (2004), and Chan and Plumb (2009).

The experiments considered here are forced with the parameters for  $\varepsilon$  and  $\gamma$  taken from Chan and Plumb (2009) and are listed in Table 1. An overview of the steady-state solutions we obtain are given in Fig. 1. Figure 1 plots the location and magnitude of the zonal wind maxima in statistically steady state averaged over the upper troposphere as a function of the strength of the stratospheric jet as controlled by  $\gamma$  and the degree of seasonality  $\varepsilon$ .

It should be noted that Fig. 1 was obtained by first interpolating the vertically averaged and pressure-weighted zonal-mean zonal wind in statistically steady

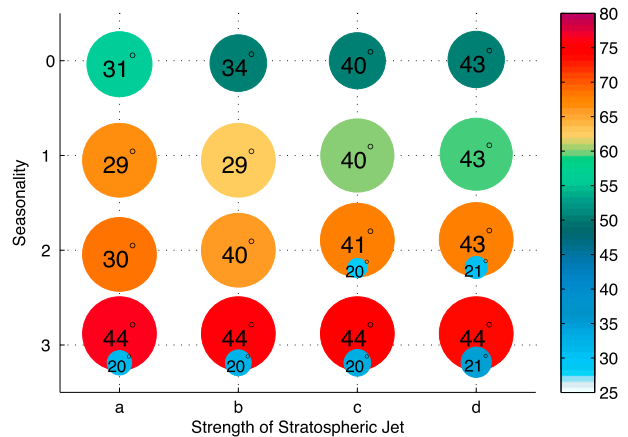


FIG. 1. Location in latitude and strength ( $\text{m s}^{-1}$ ) of maximum zonal-mean zonal wind (color and circle size) in the Northern Hemisphere averaged over the upper troposphere (514–257 hPa) for each experiment. Runs displaying a double-jet configuration are shown with secondary jet magnitude and location. Axes indicate values of the seasonal asymmetry parameter  $\varepsilon/10$  and stratospheric polar vortex strength, where letters a–d correspond to a vortex strength of  $\gamma = 1\text{--}4 \text{ K km}^{-1}$  following the convention in Table 1.

state with a cubic spline, then evaluating this fitted data for local wind maxima in latitude. This interpolation is to better resolve the jet location, as there are often only one or two grid points between a jet maximum and minimum. As a result of this interpolation, magnitudes of the jets are somewhat overestimated in Fig. 1.

The seasonality  $\varepsilon$  and strength of the stratospheric jet  $\gamma$  each influence the tropospheric circulation in a different way. Increasing  $\varepsilon$  through adjusting the equilibrium temperature in (4) shifts the latitude of maximum heating off the equator and into the Southern Hemisphere. This mimics Southern Hemisphere summer and has the effect of shifting the termination of the Northern Hemisphere Hadley circulation, and thus the location of the subtropical jet, equatorward. A figure of these equilibrium states can be found in Fig. 1 of Chan and Plumb (2009).

In Fig. 1, perturbing the equilibrium temperature by increasing the seasonality between 0 and 30 K, thus shifting the maximum heating farther into the Southern Hemisphere, forms a gradual transition from a merged jet with both eddy-driven and subtropical characteristics located at relatively low latitudes to a predominant eddy-driven jet at higher latitudes, and finally to a double-jet state where the subtropical jet splits from the eddy-driven jet. Here the subtropical jet tends to sit around  $20^\circ\text{N}$  and is much weaker, approximately  $30\text{--}40 \text{ m s}^{-1}$ , than the eddy-driven jet.

As the strength of the stratospheric jet  $\gamma$  increases, the central latitude of the jets, particularly the eddy-driven jet, moves poleward until a splitting of the subtropical

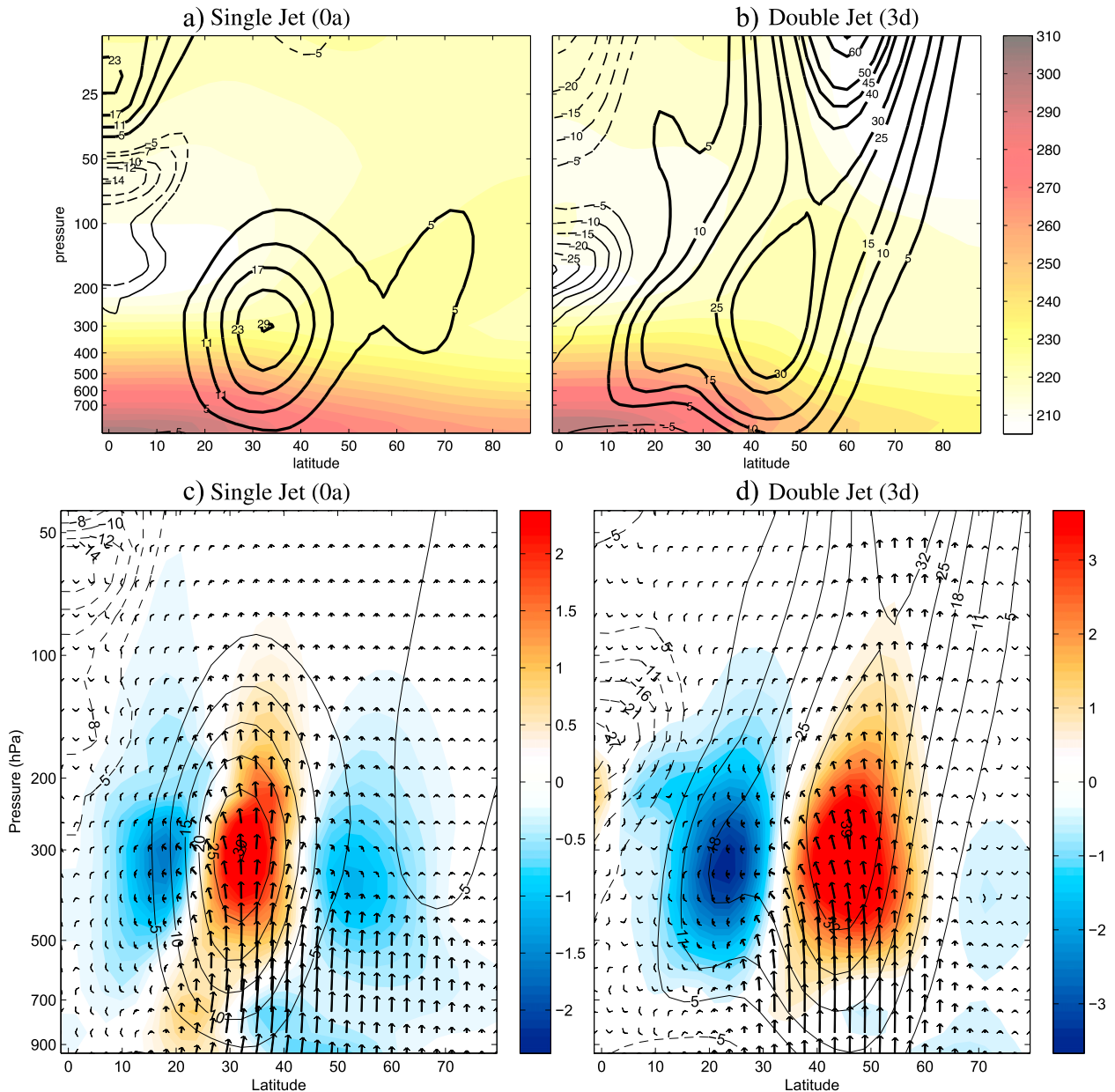


FIG. 2. (top) Contours of zonal-mean zonal wind ( $\text{m s}^{-1}$ ; black) for the Northern Hemisphere averaged over the final 512 days of integrations (a) 0a and (b) 3d. Westerly winds are thick. Colored shading is zonal-mean temperature (K). (bottom) Eddy momentum flux convergence ( $\text{m s}^{-1} \text{ day}^{-1}$ ; shaded) for integrations (c) 0a and (d) 3d, along with the full EP flux vectors (arrows). Black contours show zonal-mean zonal wind.

and eddy-driven jets occurs, as seen in cases with  $\varepsilon = 20$ - and 30-K seasonality.

Examples of a single-jet and double-jet zonal wind profile are given in Fig. 2. Figure 2a shows the zonal-mean wind profile of experiment 0a with no stratospheric jet and hemispherically symmetric heating. Figure 2b is the zonal-mean wind state for experiment 3d with a double jet in the troposphere and a strong

stratospheric jet. The generation of a mean meridional temperature gradient by increasing  $\gamma$  can be seen in the temperature field of the stratosphere with experiment 3d having a cold pool of air over the poles. As discussed, it is this meridional temperature gradient that drives the stratospheric jet.

For reference, the time-averaged fields of eddy momentum flux convergence for a single-jet case and

double-jet case are shown in Figs. 2c and 2d, respectively. Equations for eddy momentum flux convergence and the Eliassen–Palm (EP) flux vectors will be given in a later section (section 3). Eddy momentum flux convergence is centered within the eddy-driven jet in both cases and is in a more poleward position for the double-jet scenario. In the single-jet configuration, Rossby wave propagation is vertically limited to the troposphere, while some wave activity is present within the stratospheric polar vortex in the double-jet configuration. Both equatorward and poleward propagation of Rossby waves is seen in the single-jet case. Within the double-jet configuration, however, eddy momentum flux divergence is primarily located in the subtropical jet, suggesting a preferential propagation of Rossby waves into the subtropics within the double-jet configuration.

We will consider a subset of our experiments in Table 1. In this, we hold fixed the seasonality parameter  $\varepsilon$  and vary  $\gamma$  such that we obtain a transition between a single-jet state with small  $\gamma$  to a double-jet state as  $\gamma$  increases. We choose to fix  $\varepsilon = 20$  K to obtain this transition. This subset is labeled as “2a–d” in Table 1 and in the overview of the statistically steady-state jet structure in Fig. 1. For simplicity, we will focus on this subset of experiments for the remainder of the paper; however, these results hold across the entire parameter range we have tested.

### 3. Linear theory and diagnostics

OV13 found that long and short waves interact in very different manners with the subtropical and eddy-driven jet. They found that long waves had a characteristic eddy momentum flux convergence pattern that encouraged jet merger, while short waves were trapped within the eddy-driven jet waveguide and only enhanced the eddy-driven jet. These conclusions were drawn from the relative distance long and short waves may propagate meridionally, and this distance is measured by the Rossby wave refractive index.

The refractive index is a measure of wave propagation and reflection within a region. The refractive index is a function of both the wavelength of a wave and features of the mean flow, such as the mean stratification, planetary vorticity, and the zonal-mean winds. Waves preferentially propagate in regions where the refractive index is large and finite, such as those within a westerly wind core, and are reflected when the refractive index approaches 0. Similarly, waves break when the refractive index approaches positive infinity.

The refractive index squared for Rossby waves in a baroclinic atmosphere with a zonal-mean zonal wind is given by

$$n^2 = \frac{1}{\bar{U} - C} \left[ 2(\Omega + \bar{U}) - \frac{\partial^2 \bar{U}}{\partial \phi^2} + 3 \tan \phi \frac{\partial \bar{U}}{\partial \phi} - \frac{(af)^2}{p} \frac{\partial}{\partial z} \left( \frac{p}{N^2} \frac{\partial \bar{U}}{\partial z} \right) \right] - \frac{k^2}{\cos^2 \phi}, \quad (6)$$

where  $\bar{U} = \bar{u}(a \cos \phi)^{-1}$  is the zonal-mean zonal angular velocity for a zonal wind  $\bar{u}$ ,  $C = c(a \cos \phi)^{-1}$  is the zonal angular phase speed of a wave,  $\Omega$  is the planetary rotation rate,  $a$  is the radius of Earth,  $p$  is pressure,  $N^2$  is the buoyancy frequency, and  $k$  is the zonal wavenumber. The derivation of the refractive index squared, including assumptions made and the vertical coordinate  $z$  used here, is given in the appendix.

Much of this work relies on the theories of wave-mean flow interaction developed by Eliassen and Palm (1960) and expanded into the well-known Eliassen–Palm flux theory by Edmon Jr. et al. (1980). The EP flux is a zonal-mean vector with vertical and meridional components defined in spherical coordinates as

$$\mathbf{F} = F_{(\phi)} \mathbf{j} + F_{(p)} \mathbf{k}, \quad (7)$$

where

$$F_{(\phi)} = a \cos \phi \left( -\overline{v'u'} + \frac{\overline{v'\theta'}}{\theta_z} \bar{U}_z \right) \quad \text{and} \\ F_{(p)} = a \cos \phi \left\{ [f - (a \cos \phi)^{-1} (\bar{U} \cos \phi)_\phi] \frac{\overline{v'\theta'}}{\theta_z} - \overline{w'u'} \right\} \quad (8)$$

are the full EP flux vectors (Andrews et al. 1987). Here,  $f$  is the Coriolis parameter,  $\phi$  is latitude,  $z$  is a log-pressure vertical coordinate,  $v$  and  $u$  are the meridional and zonal components of the wind, respectively, and  $\theta$  is the potential temperature. Primes denote departures from the zonal average, and overbars are the zonal average.

In (8), the meridional component  $F_{(\phi)}$  is dominated by the eddy momentum flux, while the heat flux term dominates the vertical component  $F_{(p)}$ . It can be shown that  $\mathbf{F}$  represents the propagation of wave activity, thus of Rossby waves, in the atmosphere (Vallis 2006; Andrews et al. 1987). We will thus refer only to the momentum flux and heat flux terms of the horizontal and vertical components of the EP flux vectors, respectively.

We will be primarily concerned with the convergence of eddy momentum flux on the sphere, thus the horizontal component of  $\mathbf{F}$ . The scales of the horizontal and vertical components of the EP flux vector are often greatly disparate and difficult to plot as vectors. In such cases, it is often true that the vertical component of  $\mathbf{F}$  is scaled by  $(p/p_0)^k$ , where  $p_0$  is the surface reference

pressure and  $\kappa = R/c_p$  is the ratio of the dry gas constant and the heat capacity at constant pressure. The instances where the EP flux vector is plotted herein, however, have the vertical component scaled for visual clarity given our domain, resolution, and choice of graphical arrows. As this work focuses primarily on the convergence of  $\mathbf{F}$ , the vectors in these plots are shown only to get a general idea of the propagation direction and rough magnitude of Rossby waves.

#### 4. Phase speed bounds

Cospectral analyses of eddy momentum flux convergence in zonal phase speed space have been widely used in discussing the propagation of Rossby waves through a zonal-mean flow (Randel and Held 1991; Son and Lee 2005; Chen et al. 2007a; Barnes and Hartmann 2011). In this framework, eddy momentum flux convergence as a function of zonal phase speed  $c$  is bounded below the zonal-mean wind velocity (Randel and Held 1991). OV13 showed that there exists an additional minimum bound on the zonal phase speed. This minimum bound on  $c$  represents the phase speed at which a wave of a given wavelength  $k$  is reflected and gives insight into why long waves with small  $k$  may propagate farther meridionally than short waves with large  $k$ .

Bounds on the zonal phase speed for a baroclinic atmosphere with a zonal-mean flow are given by

$$\bar{u} - \frac{(1/a)(\partial\bar{q}/\partial\phi)}{f^2/(NH_0)^2 + k^2/(a^2 \cos^2\phi)} \leq c \leq \bar{u} \quad (9)$$

and can be obtained from the refractive index square in (6). The derivation for these phase speed bounds is given in the appendix. The minimum phase speed bound is obtained under the condition that the squared refractive index  $n^2$  be nonnegative. The inequalities that bound  $c$  are also derived under the assumption of a positive potential vorticity gradient. In conditions where the potential vorticity gradient is negative, such as in regions of baroclinic instability, this inequality is reversed. The parameters of (9) are the same as in (6), including one for the characteristic depth of the atmosphere  $H_0$  and the zonal-mean potential vorticity gradient  $\bar{q}$  given in (10).

Considering the sum of eddy momentum flux activity over all wavenumbers does not allow for any exploration of the wavelength-dependent minimum phase speed bound limit. Because of this, and because of two particularly striking patterns of eddy momentum flux convergence, we consider waves to be classified as either zonally long or short with zonal phase speeds given for each group given by  $1 \leq k \leq 5$  and  $6 \leq k \leq 10$ , respectively.

The cutoff between wavenumbers 5 and 6 is chosen as the lengths of these waves are roughly that of the mid-latitude deformation radius. We will additionally show that there is a relatively abrupt difference in the eddy momentum flux convergence patterns between wavenumbers 5 and 6. We choose to consider the behavior of waves based on their wavenumber because of its importance in the minimum phase speed bound; however, a similar analysis could be done separating out fast and slow modes. As a general statement, though, for a given refractive index, long waves tend to behave as slow modes while short waves behave as faster modes.

##### a. Eddy momentum flux convergence

Before considering the impact of wavelength-dependent refractive index on the meridional propagation of Rossby waves, we consider the overall patterns of eddy momentum flux convergence for all, long, and short waves. Figure 3 displays the EP flux associated with all (Fig. 3a), long (Fig. 3b), and short (Fig. 3c) waves in experiment 2c. We should note here that this work focuses on the meridional propagation of waves and thus on the horizontal component of the EP flux. Overall, both long and short waves are generated near the surface and propagate upward to approximately 200 hPa at the core of the eddy-driven jet. As can be seen from the near-surface EP flux vectors in Fig. 3, short waves tend to originate near a central latitude of 40°, while long waves tend to originate near the surface at approximately 50° latitude.

The total eddy momentum flux convergence field is largely dominated by the action of short waves, with the strongest EP flux divergence at the core of the eddy-driven jet and convergence in the core of the subtropical jet. Some limited poleward propagation of short waves is evident in Fig. 3c; however, many short waves tend to propagate toward the equator. Horizontal EP flux divergence of short waves tends to be centered at the jet altitude of 300 hPa. There is little short-wave activity below 500 hPa or above 200 hPa.

Long waves, while weaker than short waves, show a much deeper vertical structure. EP flux vectors for long waves reveal the expected upward propagation of long waves into the stratospheric jet in agreement with the theory of vertically propagating long waves (Andrews et al. 1987; Matsuno 1970). Much of the total EP flux divergence poleward of the eddy-driven jet (Fig. 3c) is associated with poleward-propagating long waves. At the jet altitude, long waves behave similarly to short waves with EP flux divergence (eddy momentum flux convergence) at the core of the eddy-driven jet and EP flux convergence (eddy momentum flux divergence) at the core of the subtropical jet.

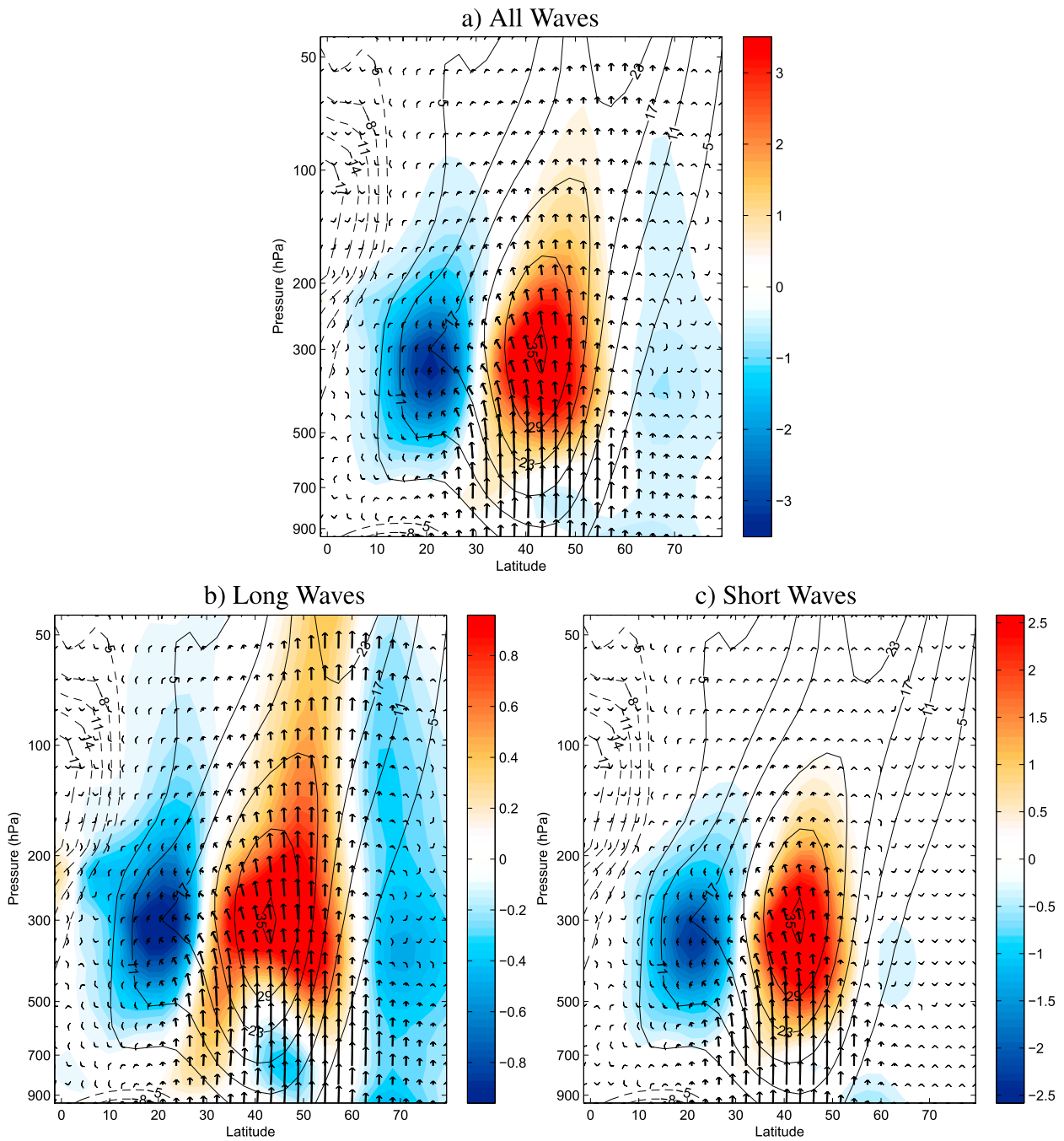


FIG. 3. Eddy momentum flux convergence ( $\text{m s}^{-1} \text{day}^{-1}$ ) summed over (a) all, (b) long, and (c) short wavelengths. Zonal wavelengths for experiment 2c are shown in colored shading. Arrows indicate full EP flux vectors. Contours of zonal-mean zonal wind are also given in black. Note the color bars are different for (a)–(c) in order to show the structure of long waves relative to short waves.

Below 500 hPa, however, long waves show a unique structure with eddy momentum flux convergence on the flanks of the eddy-driven jet and divergence within the core of the eddy-driven jet. This eddy momentum flux convergence pattern acts to decelerate and broaden the near-surface westerlies. This pattern is most consistent

with the barotropic model of OV13, revealing that the mechanisms active in that model carry over to the stratified sphere. In a mass-weighted perspective, this region constitutes half of the atmosphere; thus, these patterns of eddy momentum flux convergence are not negligible.

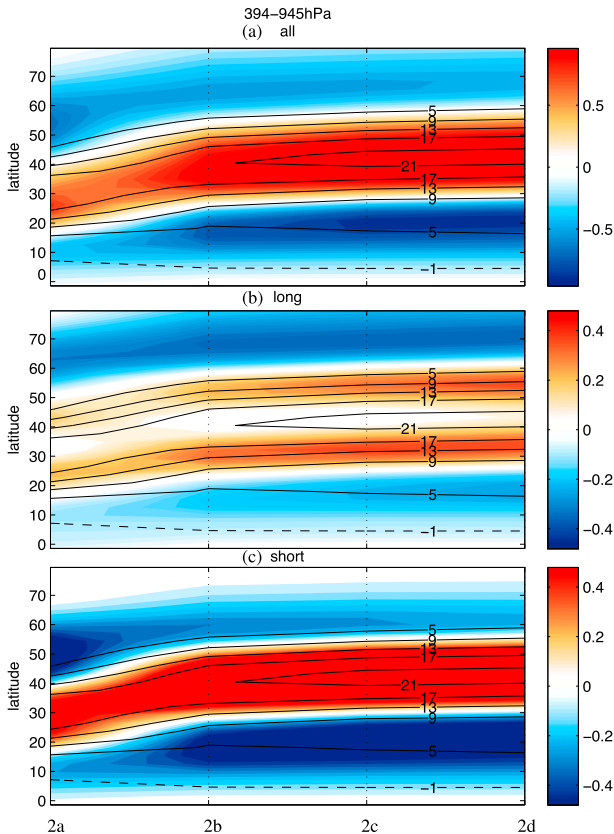


FIG. 4. Eddy momentum flux convergence (colored contours;  $\text{m s}^{-1} \text{ day}^{-1}$ ) for 2a–d summed over all phase speeds and (a) all wavenumbers, (b) long waves, and (c) short waves. Contour lines indicate zonal-mean zonal wind. Results are averaged between 945 and 394 hPa.

For a further comparison to the barotropic model of OV13, we consider the pressure-weighted vertical integral of eddy momentum flux convergence over four experiments ranging from a single-jet state to a double-jet state. The patterns of eddy momentum flux convergence associated with short waves and long waves for the experiment suite 2a–c is seen in Fig. 4.

The dominance of short waves in the total eddy momentum flux convergence (Figs. 4a,c) is again evident in the vertical integral. Total eddy momentum flux convergence follows the textbook pattern of convergence in the core of the eddy-driven jet and divergence on the flanks. Here, divergence over all waves and short waves is preferentially poleward in the single-jet case of 2a only, but this changes to the equatorward side of the jet for experiments 2b–d.

The lower-tropospheric pattern of long-wave eddy momentum flux convergence from Fig. 3 is again seen here when taking the mass-weighted vertical integral of Fig. 4b. Long waves have significant contributions to the convergence of eddy momentum flux in the regions of

strongest wind shear. Unlike short waves, long waves do not contribute much to the convergence in the center of the eddy-driven jet. Like short waves, long waves contribute to breaking both on the poleward flank of the eddy-driven jet and in the core of the subtropical jet. In the mass-weighted vertical integral, the low-level (700 hPa) long-wave eddy momentum flux divergence seen in Fig. 3b is nearly canceled by the long-wave eddy momentum flux convergence at the core of jet near 300 hPa such that long waves have a near-zero eddy momentum flux convergence in the core of the eddy-driven jet in Fig. 4b.

It should be noted that the dominance of long-wave breaking on the poleward flank of the eddy-driven jet in the mass-weighted perspective of Fig. 4b is primarily due to the low-level breaking of long waves. In the upper troposphere and at jet level, waves preferentially break on the equatorial side of the eddy-driven jet, as seen in Fig. 3b.

#### b. Wavelength dependence and cospectral diagnostics

To determine the applicability of the phase speed bounds given in (9) to horizontal eddy propagation on the sphere, we utilize the cospectral diagrams of Randel and Held (1991). We decompose the horizontal eddy momentum flux  $\overline{u'v'}$  as a function of zonal phase speed  $c$ , latitude  $\phi$ , and zonal wavenumber  $k$ . We can include the upper and lower bounds of phase speed from (9) in a plot of this cospectral amplitude for a given  $k$ , or summed over a subset of  $k$ , as a function of zonal phase speed and latitude. The minimum phase speed bound for a group of waves, such as that for long waves and short waves, will be shown as the minimum of the set. This is typically the phase speed of the longest wave, such as  $k = 1$  for long waves and  $k = 6$  for short waves.

Wave-tracing theory suggests that waves may propagate meridionally away from a region of generation until reaching a latitude at which their refractive index is either zero, a turning latitude, or infinite, a critical latitude (Hoskins and Ambrizzi 1993). To the extent that linear theory is applicable, these waves will reflect off of turning latitudes and break upon their critical latitudes. In terms of cospectral diagnostics and the phase speed bounds given in (9), the turning latitude is the location at which a propagating wave of a given phase speed  $c$  encounters a region where  $c = c_{\min}$ . Similarly, a wave reaches a critical latitude when  $c = c_{\max} = \bar{u}$ . At both of these limits, the meridional group velocity of the wave tends toward zero, preventing further propagation.

Wave breaking at critical lines leads to an irreversible eddy momentum flux out of the region of breaking. This behavior appears as a divergence of eddy momentum flux in cospectral diagrams. The combined effect of

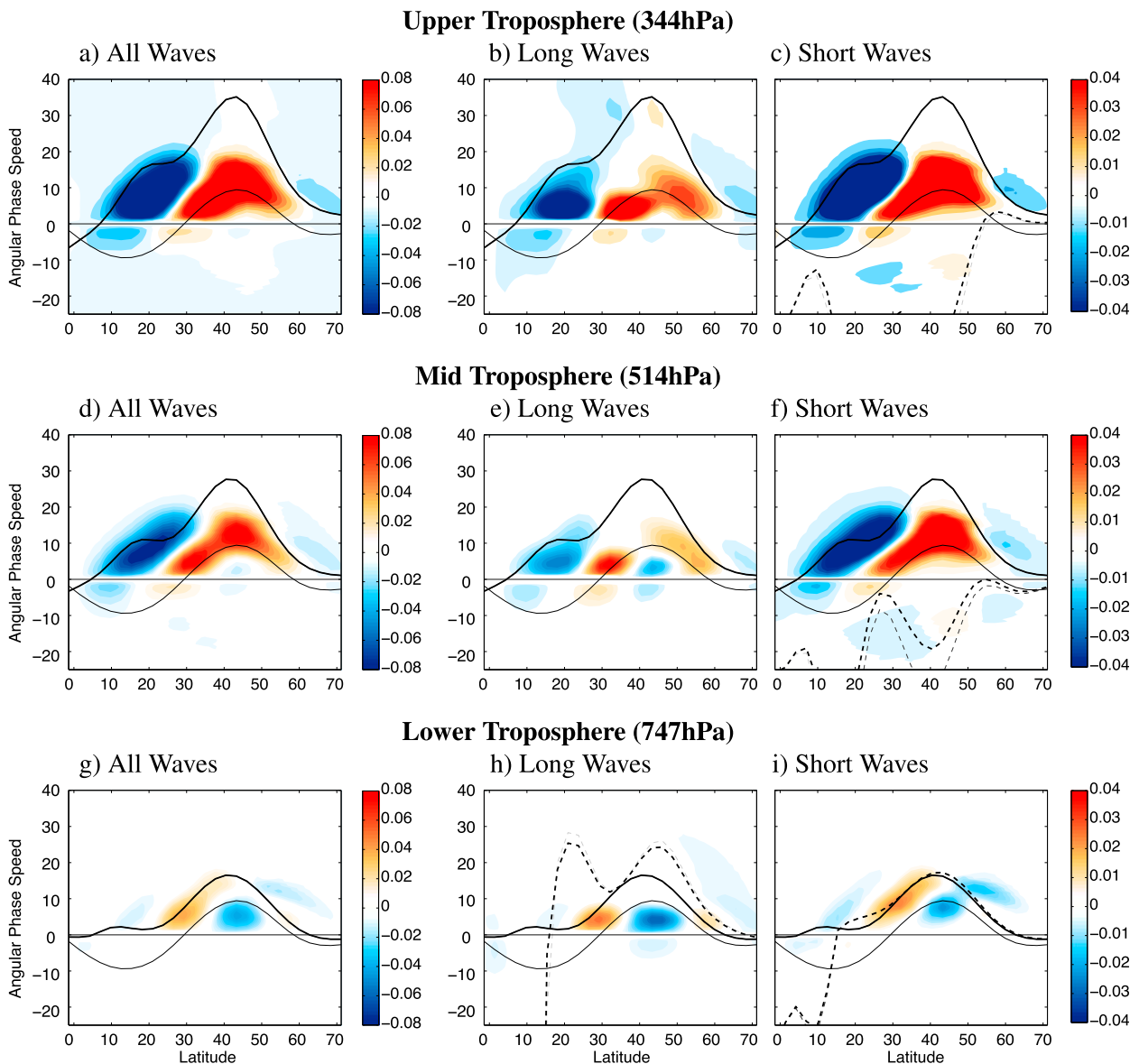


FIG. 5. Eddy momentum flux convergence cospectra ( $\text{m s}^{-1} \text{day}^{-1}$ ) of  $2c$  for (left) all waves, (right) short waves, and (center) long waves at (a)–(c) 344, (d)–(f) 514, and (g)–(i) 747 hPa as a function of latitude and phase speed. Included are the maximum and minimum phase speed bounds from linear theory in solid black thick lines and dashed lines, respectively. Black dashed lines refer to the minimum phase speed bound calculated for an isothermal atmosphere, while gray is without that approximation (see text). Surface winds are given as thin solid black lines. Long and short waves have the same color scale, which is equal to half that of all waves.

convergence of eddy momentum flux into the core of the eddy-driven jet and divergence on its flanks maintains the eddy-driven jet against dissipation.

However, waves that propagate into lower latitudes can interact with the subtropical jet, leading to, effectively, an interaction of the midlatitudes with the subtropics. It is thus of scientific interest to consider the propagation patterns of these waves, especially given the filtering effect of wavelength-dependent minimum phase speed bounds.

Eddy momentum flux convergence decomposed into phase speed and latitude for experiment 2c at three altitudes is shown in Fig. 5. As expected, nearly all eddy momentum flux activity is restricted below the maximum phase speed bound. Over all wavenumbers, wave breaking occurs preferentially at the latitude of the subtropical jet and secondarily on the poleward flank of the eddy-driven jet. Here, surface winds restrict the minimum phase speed of waves more so than  $c_{\min}$  in (9), as the surface winds tend to be faster than the minimum

phase speed bounds for the wavelengths considered here. This is in contrast to the barotropic model of OV13, where, in the absence of a lower-layer wind, the minimum phase speed was the dominant lower bound.

The cospectral diagnostics of short and long waves seen in Fig. 5 will be discussed for long and short waves separately below. The vertical levels are chosen to be near the core of the jet in the upper troposphere (344 hPa), in the midtroposphere (514 hPa), and in the baroclinically unstable layer in the lower troposphere (747 hPa). Eddy momentum flux convergence patterns in the upper- and midtropospheric depths (Figs. 5a–f) are similar; however, those at the midtropospheric depth (Figs. 5d–f) most resemble that of the mass-weighted vertical integral of Fig. 4.

It should be noted that the lower troposphere (Figs. 5g–i) is within the baroclinically unstable region of the troposphere; thus, the minimum phase speed bounds  $c_{\min}$  for long and short waves are, in fact, greater than the upper bound  $c_{\max}$  from (9). This reversal of bounds occurs in regions where the mean potential vorticity gradient is negative because of the baroclinic component of the mean potential vorticity gradient. Nonetheless, this layer is shown for completeness; however, theories of wave propagation similar to Hoskins and Ambrizzi (1993) and those presented here may not apply within this layer, as it is inherently unstable. As such, the discussion of short-wave and long-wave propagation dynamics will focus on the cospectral analysis of the upper- and midtropospheric depths.

### c. Short waves

From Fig. 5, we again see that the spectrum of eddy momentum flux convergence is dominated by short waves at all levels. With the exception of the lower troposphere, short waves behave as expected, wherein waves are generated near the core of the eddy-driven jet via near-surface baroclinic instability. Unlike the  $\beta$ -plane model of OV13, short waves do not break symmetrically across the axis of the eddy-driven jet because of the reduction of the planetary vorticity gradient near the poles.

Short waves propagate preferentially into the subtropical jet region, as can be seen from the strong, short-wave eddy momentum flux divergence in these regions in Fig. 5. This indicates that short waves interact with the subtropical jet and, thus, the tropical circulation. This is strongly contrasting the results of OV13, where short waves were largely confined to the eddy-driven jet because of the presence of a turning latitude in the eddy-driven jet region.

The effect of turning lines, or regions with a weak potential vorticity gradient, is not as evident here as on

the  $\beta$ -plane model of OV13. OV13 found that the interjet potential vorticity gradient was sufficiently weak to prevent the horizontal propagation of short waves because of the relatively high minimum phase speed bound there. When the interjet potential vorticity gradient is weak,  $c_{\min} \approx c_{\max}$  for short waves. This is equivalent to saying short waves encounter a reflecting line at latitudes where  $c(k) = c_{\min}$ .

Here, however, the interjet potential vorticity gradient is sufficiently strong as to permit the propagation of short waves into the subtropical jet. The effect of the minimum phase speed bound, and thus reflection, does not appear to play as large of a role in a stratified, spherical domain. Rather, the surface winds determine the minimum phase speed of short waves. The critical lines, or upper phase speed bounds, limit the meridional propagation of short waves more so than the reflecting line or the minimum phase speed bound.

Nonetheless, it should be noted that the forcing of short waves here differs from that in OV13. The barotropic  $\beta$ -plane model of OV13 includes the excitation of waves of wavenumbers 6–15; thus, short waves were generated by the imposed stirring of the vorticity field. Here, short waves are generated from baroclinic instability within the model storm tracks, much like that of Earth's atmosphere. Despite the differences in forcing, geometry, and stratification, the eddy momentum flux convergence associated with short waves in this model is similar to that of OV13. Additionally, the minimum phase speed bound may be important for circulations where  $c_{\min}$  was greater than the surface winds, such as for either very weak surface winds or for very short waves.

### d. Long waves

Long waves, or those with zonal wavenumbers between 1 and 5 are associated with slowly moving disturbances propagating predominantly eastward at phase speeds less than  $10 \text{ m s}^{-1}$ ; however, there is some evidence of westward-moving waves in Fig. 5. Long waves have such small minimum phase speed bounds that turning latitudes are not significant in their propagation. In the case of a double-jet atmosphere, long waves may propagate freely between them with little interruption. The interjet minimum in the potential vorticity gradient is still transparent to long waves.

Long-wave eddy momentum flux convergence is characterized by regions of convergence (wave generation) on the poleward flank of the eddy-driven jet and in the interjet region and divergence (wave breaking) in the core of both the subtropical and eddy-driven jets (Fig. 5). Eddy momentum flux convergence is dominated by zonal wavenumber  $k = 5$ , as seen in Fig. 6;

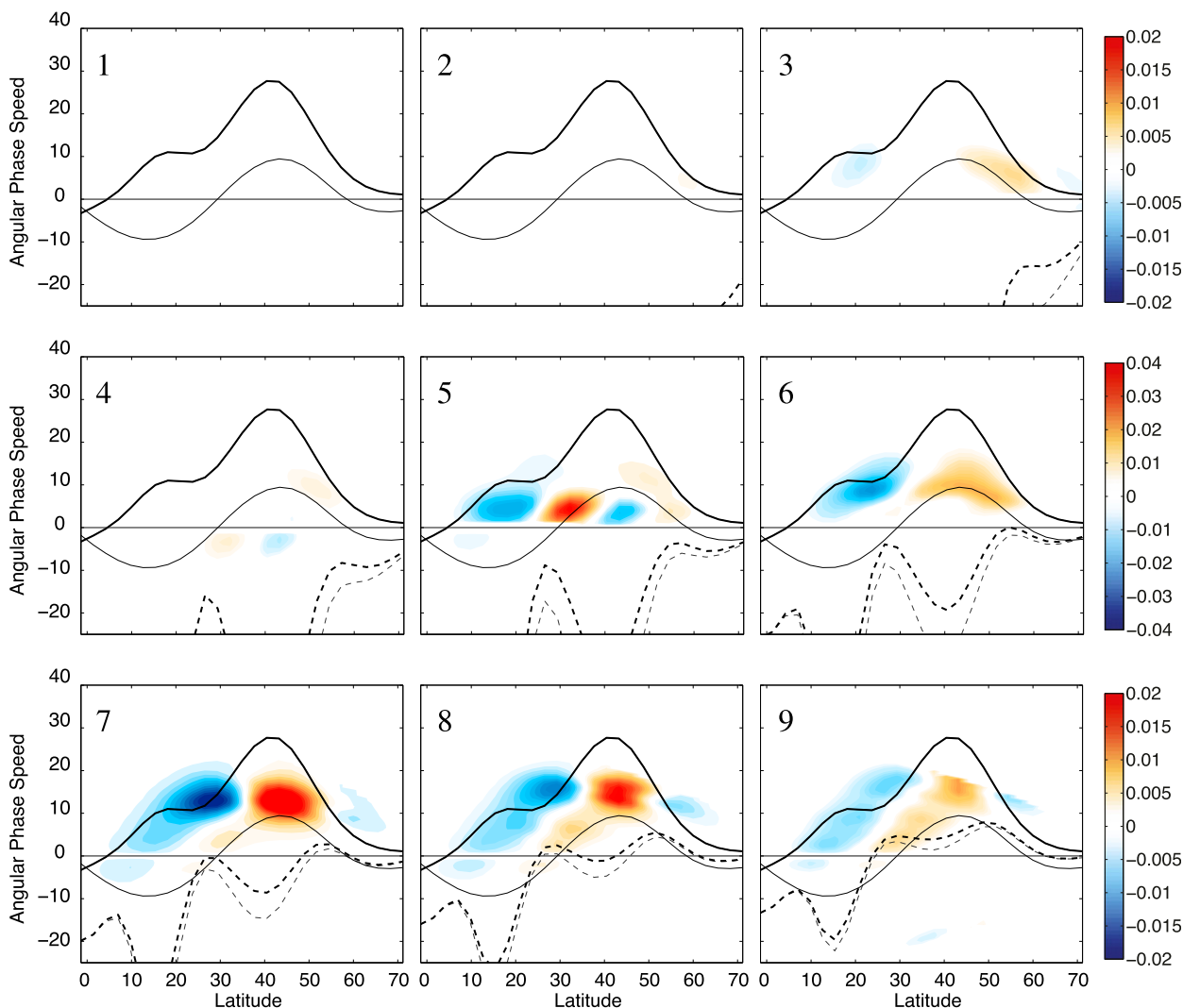


FIG. 6. Eddy momentum flux convergence cospectra ( $\text{m s}^{-1} \text{day}^{-1}$ ) of experiment 2c for individual wavenumbers, given in the upper-left corner of each plot, as measured at 514 hPa. Note that the color bar for dominant wavenumbers 4–6 is twice that of wavenumbers 1–3 and 7–9.

however, there are some weak patterns from zonal wavenumbers  $k = 3$  and 4. The longest waves,  $k = 1$  and 2, are not evident in the eddy momentum flux cospectra at 514 hPa shown in Fig. 6, in part because of their ability to penetrate much higher into the troposphere and even stratosphere before being refracted meridionally.

These extremely long waves, at  $k = 1$  and 2, are not negligible overall and have been noted to be extremely important in the coupling of the troposphere with the stratosphere. However, as we are focused on waves propagating meridionally between the double jets in the tropopause, these waves do not contribute greatly to our discussion here.

The pattern of eddy momentum flux convergence here for long waves opposes that of short waves. Long waves tend to act against the action of short waves,

which typically decelerate the interjet region and accelerate the eddy-driven jet core. This pattern effectively erodes the double-jet state and has a tendency to draw the atmosphere back to that of a single, merged jet. This is also a characteristic of the interjet disturbances of Kim and Lee (2004), suggesting that the long waves in this study are related to IJDs. Like the IJDs of Kim and Lee (2004), these waves are not likely a part of the typical baroclinic wave life cycle like the short waves considered here.

### 5. Surface friction and long-wave eddy momentum flux

Jet latitude can be controlled by a number of factors beyond the two, seasonality and strength of the

stratospheric jet, including the effects of surface friction, as described by [Chen et al. \(2007b\)](#). Changing surface friction can adjust the vertical structure of the wind field, leading to a more barotropic atmosphere under weak friction and a more sheared profile under increased friction. We consider here a small test to examine the sensitivity of the wave–mean flow interaction described previously to different surface friction damping rates from the model's initial damping time scale of  $1 \text{ day}^{-1}$  to a reduced time scale of  $0.57 \text{ day}^{-1}$ , herein called the “weak surface damping” case, and an increased Rayleigh damping time scale of  $4 \text{ day}^{-1}$  or “strong surface damping.” The control case considered is that of 3b, an experimental case with a strong double jet in statistically steady state ([Fig. 1](#)) with a slightly stronger seasonality and a weaker stratospheric jet than the previously considered test case of 2c.

[Figure 7](#) displays the long-wave eddy momentum flux convergence for the strong, control, and weak surface damping. We see that the long-wave control case for 3b looks similar to that of 2c previously shown in [Fig. 3b](#). Both of these experiments have characteristics of a double jet in the upper troposphere, and both display the pattern of lower-tropospheric long-wave eddy momentum flux divergence at the core of the eddy-driven jet and divergence in the regions of strong meridional shear on the flanks of the jets.

As expected, increasing the surface friction rate decreases the magnitude of the surface winds. In the strong-drag case of [Fig. 7b](#) the surface winds are near zero, while in the decreased-drag case of [Fig. 7c](#), the winds are about  $5 \text{ m s}^{-1}$  greater than that of the control case.

While the change in surface wind speeds is unsurprising, increasing the surface friction rate as in [Fig. 7b](#) leads to a dramatic collapse of the double-jet structure. This is consistent with the surface friction experiments of [Chen et al. \(2007b\)](#). In [Chen et al. \(2007b\)](#), increasing (decreasing) the surface friction shifts the surface westerlies equatorward (poleward) and with it the eddy-driven jet. Also expected in [Fig. 7b](#) is the reduction in wind magnitude.

Surprisingly, though, increasing the surface friction effectively removes the anomalous long-wave eddy momentum flux pattern seen previously. Instead, long waves act similarly to short waves in that they accelerate the jet core, decelerate the flanks, and are confined to the mid- to upper troposphere. This may suggest that the anomalous pattern of long-wave eddy momentum flux convergence in the near surface of experiment 2c in [Fig. 3](#) and of experiment 3c in [Fig. 7a](#) requires a double-jet zonal-mean flow.

Meanwhile, decreasing the surface friction, as in [Fig. 7c](#), enhances the pattern relative to the control case

in [Fig. 7a](#). In this weak drag case, the surface winds are shifted poleward and strengthened, and the double-jet structure is enhanced. Along with the enhancement of the double-jet structure is the strengthening of the long-wave eddy momentum flux convergence pattern in the lower half of the troposphere.

The strengthened eddy momentum flux convergence pattern seen in [Fig. 7c](#) relative to the control case is consistent with increased zonal-mean zonal winds, particularly in the lower troposphere. As in [Chen et al. \(2007b\)](#), reducing the surface friction leads to a more barotropic atmosphere where vertical shears are weakened and horizontal shears are enhanced. The long-wave eddy momentum flux convergence again appears in regions of strong meridional shear in the zonal-mean zonal wind.

The dependence of the long-wave eddy momentum flux convergence pattern on the structure of the jets, specifically on the presence of a single or double jet in the zonal mean, will be explored further using a composite analysis of single-jet and double-jet days within a single integration.

## 6. Composite analysis of the development of a double jet

A unique feature of the double-jet atmospheric state is that it has the potential for strong meridional shears in the zonal-mean zonal wind between the eddy-driven and subtropical jets. In [OV13](#), these meridional shears were strong enough to occasionally lead to an overturning of the potential vorticity gradient, thus satisfying the Rayleigh–Kuo criterion for barotropic instability. It was thus hypothesized in [OV13](#) that the anomalous long-wave eddy momentum flux convergence patterns may be associated with barotropic instability and the presence of these strongly sheared interjet regions when the zonal mean takes on a double-jet state. As these patterns persist in the stratified, spherical model here, we investigate the relationship between this long-wave behavior and the structure of the zonal-mean zonal winds.

There exists a large degree of natural variability within any given steady-state integration considered in this study, not unlike the observed atmosphere, such that for one experiment we may have both strong single-jet and strong double-jet days. We may take advantage of this internal variability and consider a composite analysis over single- and double-jet days within a single experiment to directly compare the role of long- and short-wave eddy momentum flux to the jet state without changing the overall forcing parameters of seasonality or the strength of the stratospheric jet. By identifying instances of a particularly strong double jet, we may also

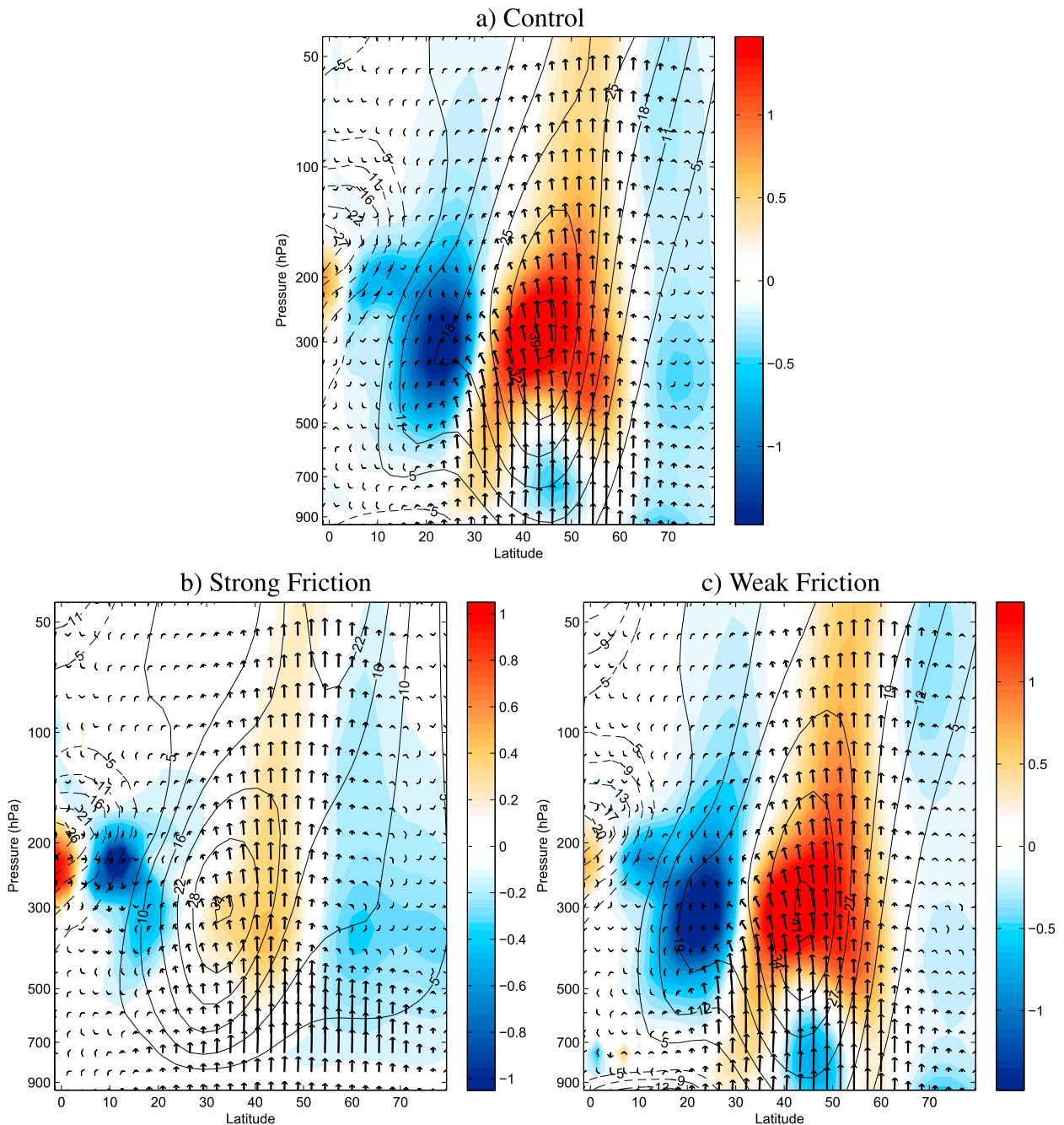


FIG. 7. Eddy momentum flux convergence ( $\text{m s}^{-1} \text{day}^{-1}$ ; colored contours) summed over long zonal wavelengths for three experiments with surface friction of (a)  $1 \text{ day}^{-1}$  (control), (b)  $4 \text{ day}^{-1}$  (strong drag), and (c)  $0.57 \text{ day}^{-1}$  (weak drag). Arrows indicate full EP flux vectors. Contours of zonal-mean zonal wind are shown in black for reference. Control experiment for this set is experiment 3b.

consider the role of wave driving in the development and maintenance of the double-jet structure.

To consider a composite analysis of these circulation features, however, we must first identify single-jet and double-jet days for an experiment. These days are distinguished by the barotropic component of the interjet potential vorticity gradient. This measure is

at a minimum during double-jet days and a maximum during single-jet days.

#### a. Temporal variability within integrations

Before considering the barotropic component of the total potential vorticity gradient, it is useful to describe the model's baroclinic regions by discussing the full

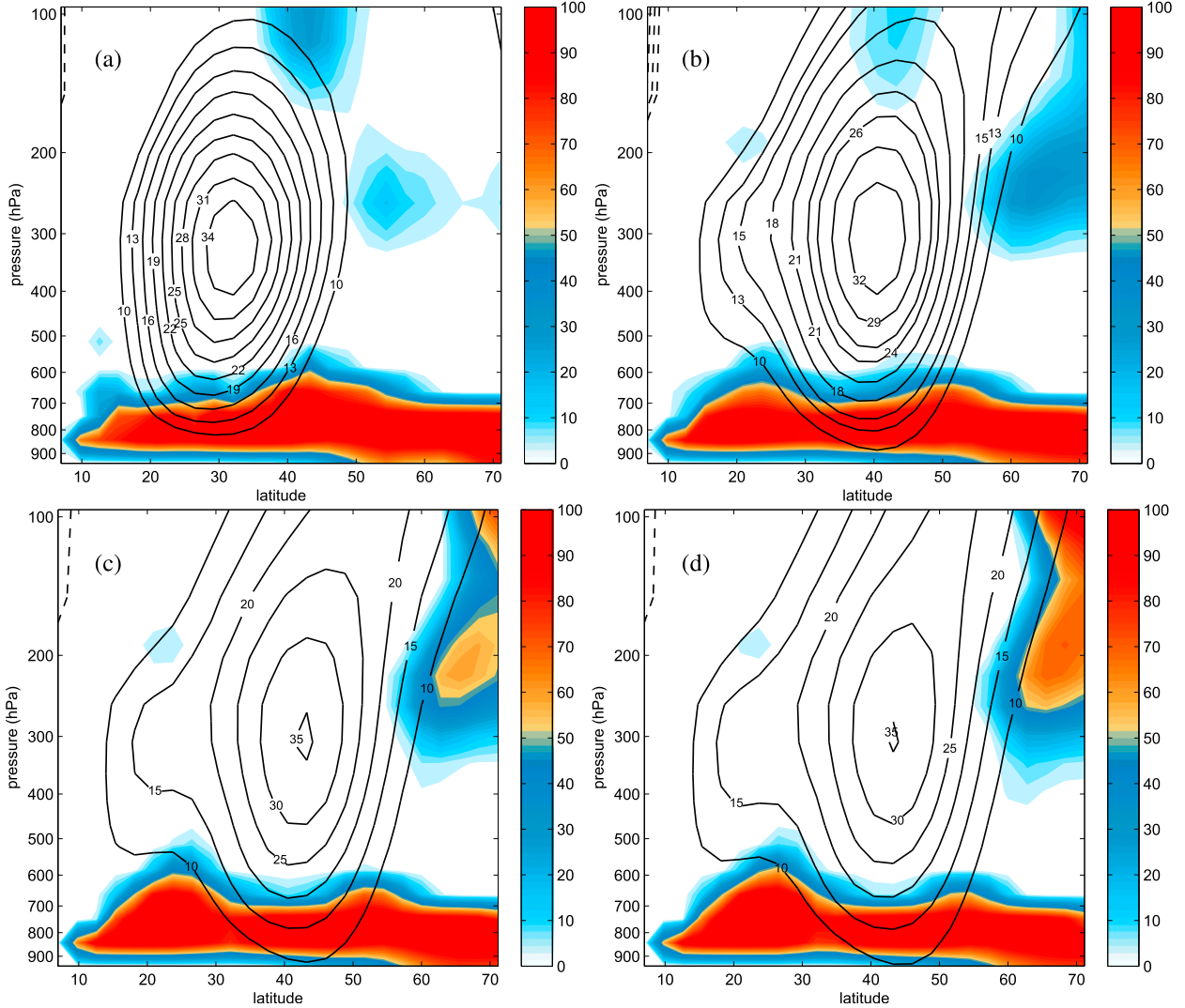


FIG. 8. Percentage of days out of the total steady-state integration (frequency) in which the zonal-mean total potential vorticity gradient [see (10)] is less than zero (colors) for experiments 2a–d. The contours of zonal-mean zonal wind are shown in black. Panels differ in the strength of the stratospheric vortex (see Table 1), a parameter that, as it strengthens, leads to the development of a double-jet state, as shown.

meridional potential vorticity gradient on the stratified sphere. The zonal-mean meridional potential vorticity gradient is given by

$$\frac{\partial \bar{q}}{\partial \phi} = \cos \phi \left[ 2(\Omega + \bar{U}) - \frac{\partial^2 \bar{U}}{\partial \phi^2} + 3 \tan \phi \frac{\partial \bar{U}}{\partial \phi} - \frac{(af)^2}{p} \frac{\partial}{\partial z} \left( \frac{p}{N^2} \frac{\partial \bar{U}}{\partial z} \right) \right]. \quad (10)$$

In interjet region,  $\bar{q}_\phi$  is at a midtroposphere minimum because of the strong meridional curvature in the profile of zonal-mean zonal wind [i.e., the second derivative of  $\bar{U}$  in the potential vorticity gradient given in (10)].

Following the Rayleigh–Kuo criterion for instability, the classic case of baroclinic instability arises when  $\bar{q}_\phi$  of (10) changes sign within the domain. This typically occurs in the lower levels because of the strength of the vertical shear term of (10), and that is indeed the case here.

The overturning of the potential vorticity gradient, and thus the location of the baroclinic regions within the model, can be seen by considering the frequency of overturning of (10) across experiments 2a–c in Fig. 8. As the double-jet structure emerges, a negative potential vorticity gradient becomes more frequent in the interjet region at approximately 20°–30° latitude and between the surface and 600 hPa, owing in part to the increasing

zonal wind shear and the weakening of the barotropic component of  $\bar{q}_\phi$  given in (10).

The barotropic component of the mean potential vorticity gradient in (10) is given as

$$\frac{\partial \bar{q}}{\partial \phi} = \cos \phi \left[ 2(\Omega + \bar{U}) - \frac{\partial^2 \bar{U}}{\partial \phi^2} + 3 \tan \phi \frac{\partial \bar{U}}{\partial \phi} \right]. \quad (11)$$

It is important to note that the barotropic potential vorticity gradient in (11) neglects the vertical curvature of the zonal-mean zonal wind found in (10), a component that is significant near the surface of the mid-latitudes and is associated with baroclinic instability. That is to say, we focus on the potential vorticity gradient absent any effects of vertical shear. This is similar to considering either an individual layer of the atmosphere or meridional shear over the integrated tropospheric depth.

We consider this barotropic component in order to relate these results back to those of the barotropic model of OV13. Additionally, by focusing on the barotropic component of the potential vorticity gradient, we can identify days with a strong meridional shear of the zonal-mean zonal wind in the interjet region that is indicative of a double jet.

Analysis of the frequency of overturning of the zonal-mean barotropic component of the potential vorticity gradient of (11) is seen in Fig. 9 for experiments 2a–c spanning both single- and double-jet mean flows. We find there are indeed days where the barotropic component of the potential vorticity gradient changes sign in the interjet region at approximately 25° latitude and at an altitude of 400 hPa; however, this is intermittent and only occurs on approximately 30% of the days of the statistically steady-state integration. These intermittent days of very weak barotropic potential vorticity are days within statistically steady state where the double jet is the most pronounced.

### b. Binning methodology

Days with an extreme positive or negative interjet potential vorticity gradient are identified using a time series of the zonal and daily averaged barotropic potential vorticity gradient given in (11) for experiment 3c. This time series is then averaged vertically over pressure levels to identify the interjet latitude at which the horizontal potential vorticity gradient most often changes sign. Single- and double-jet days are identified as those greater and less than 1.5 standard deviations above the statistically steady-state time mean. A similar composite analysis is used in Kim and Lee (2004) to analyze the development of interjet disturbances.

### c. Long waves

Long-wave eddy momentum flux in integrations with double-jet mean states had a characteristic pattern of divergence at the core of the jets and convergence on the flanks of the eddy-driven jet (Fig. 4b, for example). We see in Fig. 10c that this pattern is starkly enhanced in the composite over days with a double jet within the single-integration 3c. The composite over single-jet days (Fig. 10a) has a pattern very similar to that of the time mean (Fig. 10b), despite the fact that the time mean indeed has a separate eddy-driven and subtropical jet.

In Figs. 10d and 10f, we consider the momentum flux convergence anomalies to the mean by taking the difference between the single- and double-jet composites and the time average. The long-wave eddy momentum flux convergence anomalies on single-jet days (Fig. 10d) show an enhanced convergence of momentum into the poleward flank of the eddy-driven jet and divergence along the core of the subtropical jet and within the interjet region. This suggests that waves are accelerating the poleward flank of the eddy-driven jet, thus broadening it, while damping the subtropical jet leading to a single, dominant eddy-driven jet at a slightly more equatorward latitude than in the time mean.

Meanwhile, the composite over double-jet days in Fig. 10f has a pattern of anomalies that opposes that of the control case. Here, long waves are generated on both the poleward flank of the eddy-driven jet and within the interjet region. Relative to the time mean (Fig. 10e), wave-driven mean-flow acceleration is reduced at the core of the eddy-driven jet and enhanced in the subtropical jet.

### d. Short waves

Short waves, as shown in Fig. 11, are not as strongly influenced by structure of the single- or double-jet state as long waves. Composites over both single- (Fig. 11a) and double-jet (Fig. 11c) days are very similar to the time mean (Fig. 11b) with few notable differences. The composite over single-jet days (Fig. 11a) has a convergence region that is shifted slightly equatorward relative to the mean. Double-jet days (Fig. 11c) have relatively weaker convergence in the core of the eddy-driven jet and less breaking within the subtropical jet.

In the composite over single-jet events (Fig. 11d), there is an equatorward shift of the short-wave eddy momentum flux convergence region within the eddy-driven jet centered around 40° and a slight strengthening of short-wave eddy momentum flux divergence within the subtropical jet. There is a slight reduction in wave breaking, or eddy momentum flux divergence, within the subtropical jet in the composite over double-jet

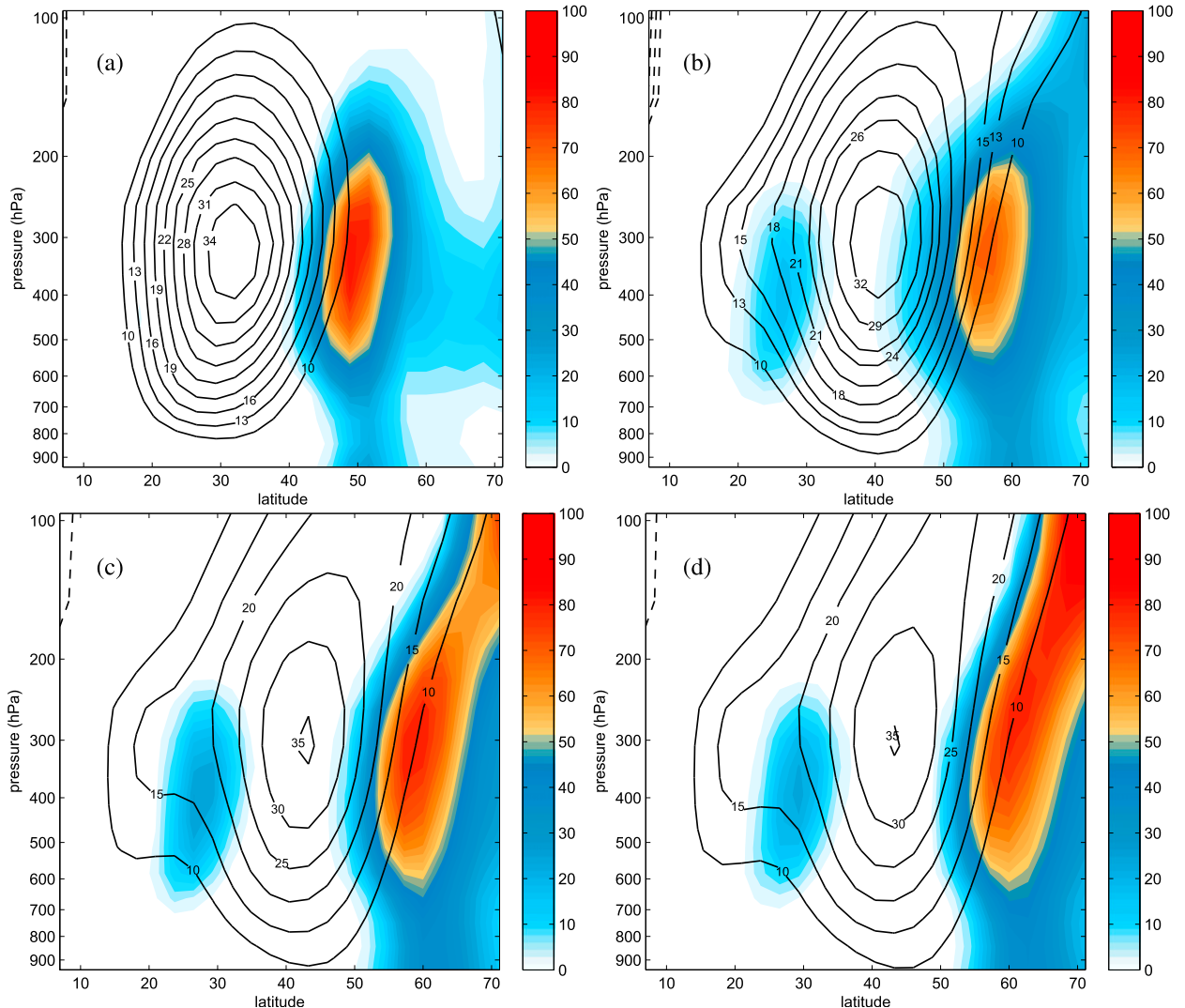


FIG. 9. Percentage of days out of the total steady-state integration (“frequency”) in which the zonal-mean barotropic component of the potential vorticity gradient [see (11)] is less than zero (colors) for experiments 2a–d. The contours of zonal-mean zonal wind are shown in black. Panels differ in the strength of the stratospheric vortex, a parameter that, as it strengthens, leads to the development of a double-jet state, as shown.

events (anomalous positive activity in the subtropical jet region of Fig. 11f), suggesting a reduction of equatorward-propagating short waves. This agrees well with the idea that the presence of a weak interjet potential vorticity gradient limits the propagation of short waves as a result of the presence of turning latitudes.

#### e. Development of the double jet

In addition to considering the structure of the zonal-mean zonal wind and eddy momentum flux convergence over a composite of strong single- and double-jet days, composite analysis allows us to consider the development of these states in time and the role that long and short waves play in the maintenance of the zonal wind

structure. In particular, we may consider here the eddy momentum flux convergence leading up to a strong double-jet event, here occurring at the composite day 0, and how, once a double jet is formed, it steadily maintains that structure at times upward of 20 days.

A time-lag composite of the anomalous zonally averaged, vertically integrated zonal velocity field (Fig. 12a) and total eddy momentum flux convergence for all, long, and short waves (Figs. 12b–d) for extreme double-jet days within experiment 3c is shown in Fig. 12. Day 0 indicates the day of minimum of the interjet horizontal potential vorticity gradient. From the zonal-mean winds of Fig. 12a, we can see that the central latitudes of the eddy-driven and subtropical jets are at approximately

### Full Fields: Long Wave Eddy Momentum Flux Convergence

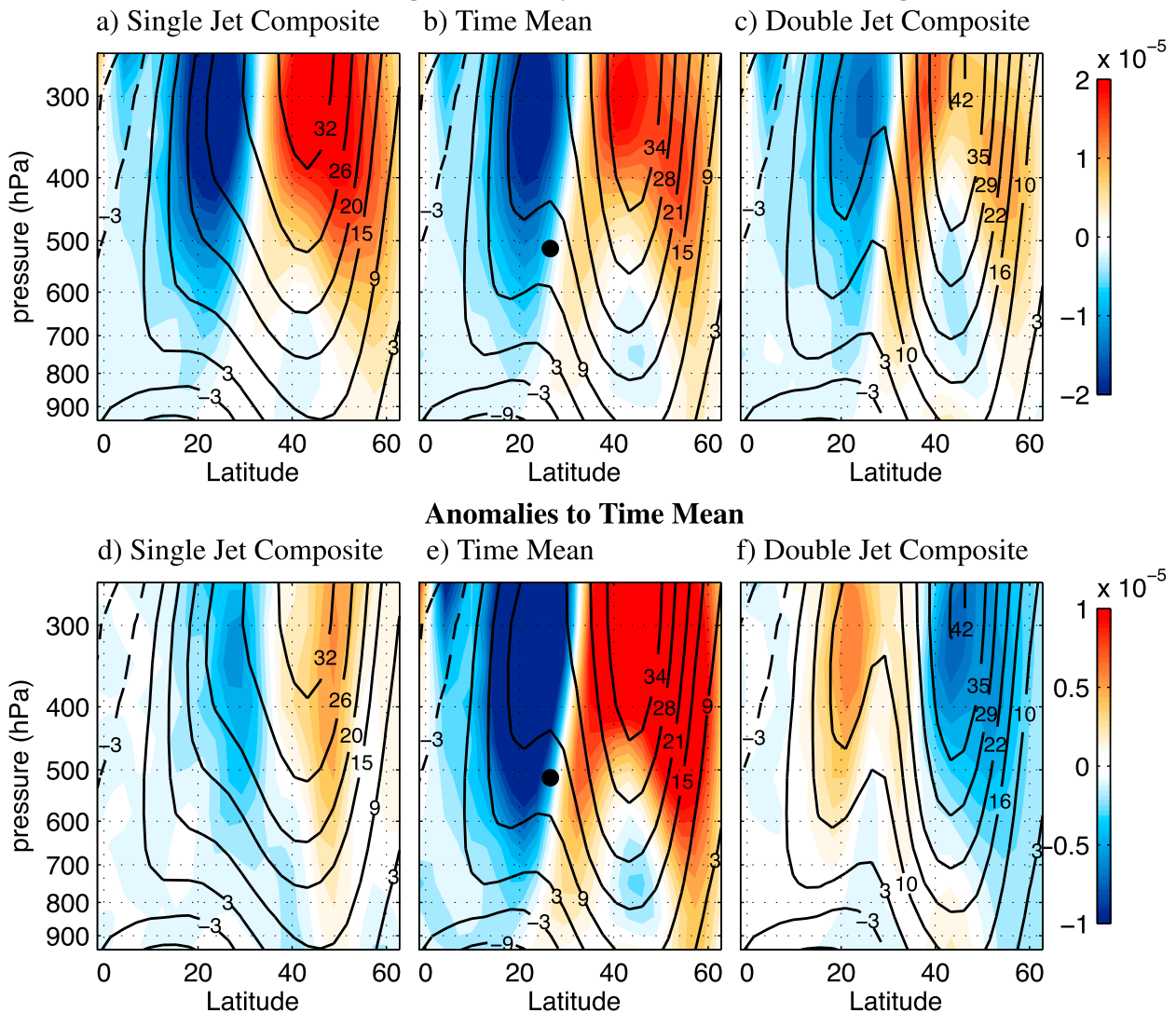


FIG. 10. Long-wave eddy momentum flux convergence ( $\text{m s}^{-1} \text{day}^{-1}$ ) binned according to the strength of the horizontal interjet potential vorticity gradient in colored contours for (a),(d) single-jet; (b),(e) time-mean; and (c),(f) double-jet days. Zonal wind fields are given in black contours. (top) The full fields and (bottom) deviation from the time mean. Note the time mean for this particular experiment is the same in (b) and (e); however, the color bar changes magnitude. The bullet point indicates the location at which the horizontal potential vorticity gradient is evaluated for composite purposes.

$45^\circ$  and  $20^\circ\text{N}$ , respectively, while the interjet location is at approximately  $27^\circ\text{N}$ . At day 0, the vertically averaged horizontal potential vorticity gradient calculated using (11) is only weakly positive.

The zonal-mean winds show an anomalous strengthening of the eddy-driven jet center and weakening of the winds in the interjet region preceding the minimum horizontal potential vorticity gradient from approximately day  $-5$  to day  $-1$ . Total eddy momentum flux convergence for this time period (Fig. 12b) shows an anomalous convergence preceding the strengthening of

the eddy-driven jet. This anomalous eddy momentum flux convergence is driven by an anomalous strengthening of both long- and short-wave eddy momentum flux convergence between  $40^\circ$  and  $60^\circ\text{N}$ . While the overall time-mean short-wave eddy momentum flux convergence is larger than that of long waves within the eddy-driven jet, the anomalous long-wave eddy momentum flux convergence is slightly larger than the short-wave eddy momentum flux convergence preceding day 0.

Both long and short waves contribute an anomalous divergence within the interjet region, suggesting a weak

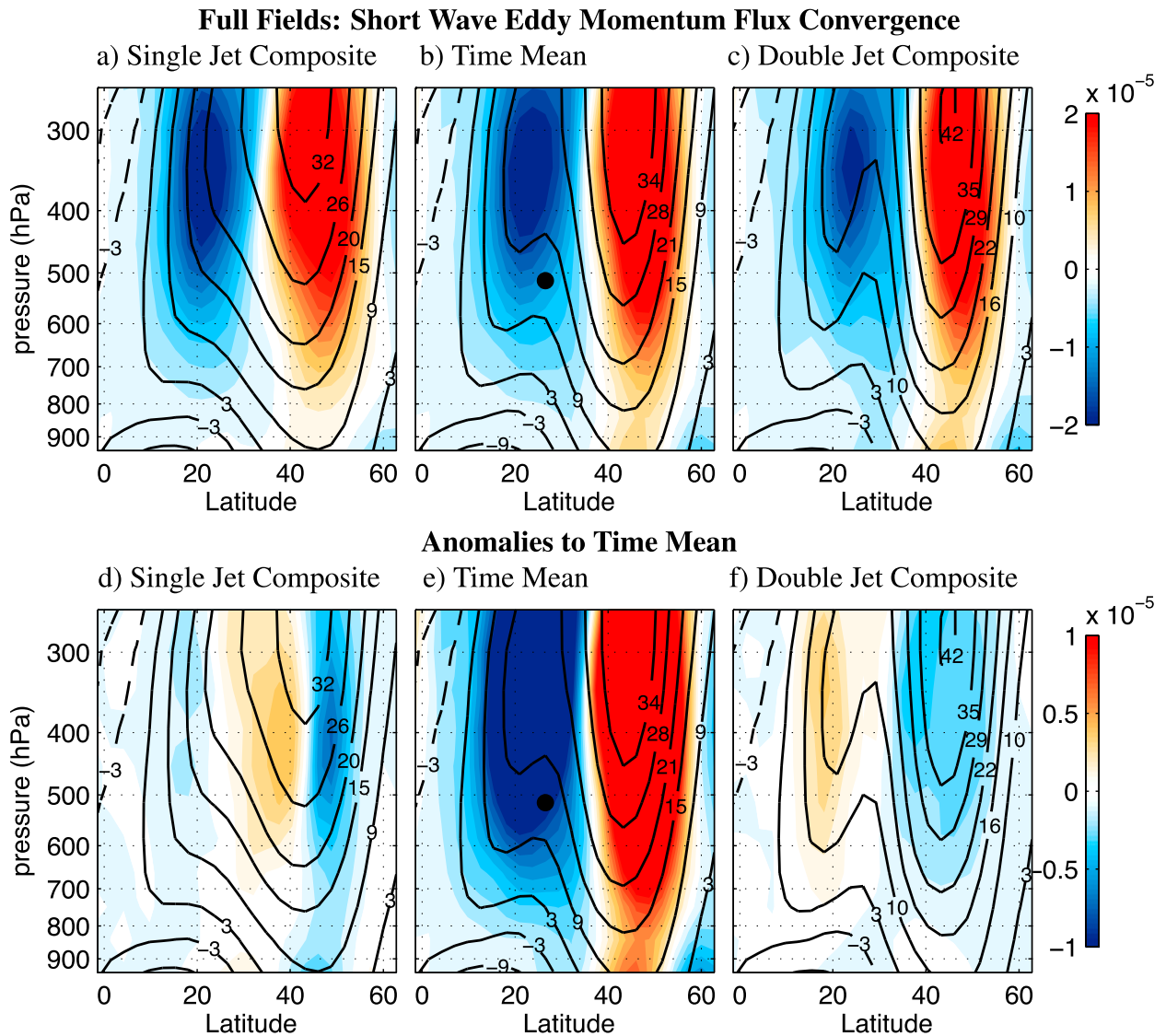


FIG. 11. Short-wave eddy momentum flux convergence ( $\text{m s}^{-1} \text{ day}^{-1}$ ) binned according to the strength of the horizontal interjet potential vorticity gradient in colored contours for the (a),(d) single-jet, (b),(e) control, and (c),(f) double-jet regimes. Zonal wind fields are given in black contours. (top) The full fields and (bottom) deviation from control. Note the control case is the same in (top) and (bottom); however, the color bar changes magnitude. The bullet point indicates the location at which the horizontal potential vorticity gradient is evaluated for composite purposes.

poleward shift in the center of wave generation; however, short-wave eddy momentum flux convergence shows little overall changes in latitudinal location from average preceding day 0. It should be noted that both long waves and short waves contribute to the anomalous eddy momentum flux convergence preceding day 0; however, the magnitude of the anomaly to the time mean of long-wave eddy momentum flux convergence is slightly larger in magnitude than that of the anomalous short-wave eddy momentum flux convergence.

The days following day 0 reveal almost a complete reversal of the anomalous eddy momentum flux convergence

patterns for both long and short waves. Eddy momentum flux convergence is enhanced in the interjet region and strongly weakened in the eddy-driven jet region, suggesting waves of both wavelengths are accelerating the winds in the interjet region at the expense of the eddy-driven jet core.

Long-wave eddy momentum flux is, in fact, divergent (negative) at day 0 and for the 5 days following within the eddy-driven jet core, suggesting that long waves are acting to weaken the winds in this region. Long-wave eddy momentum flux convergence changes sign within the eddy-driven jet core from strongly convergent to

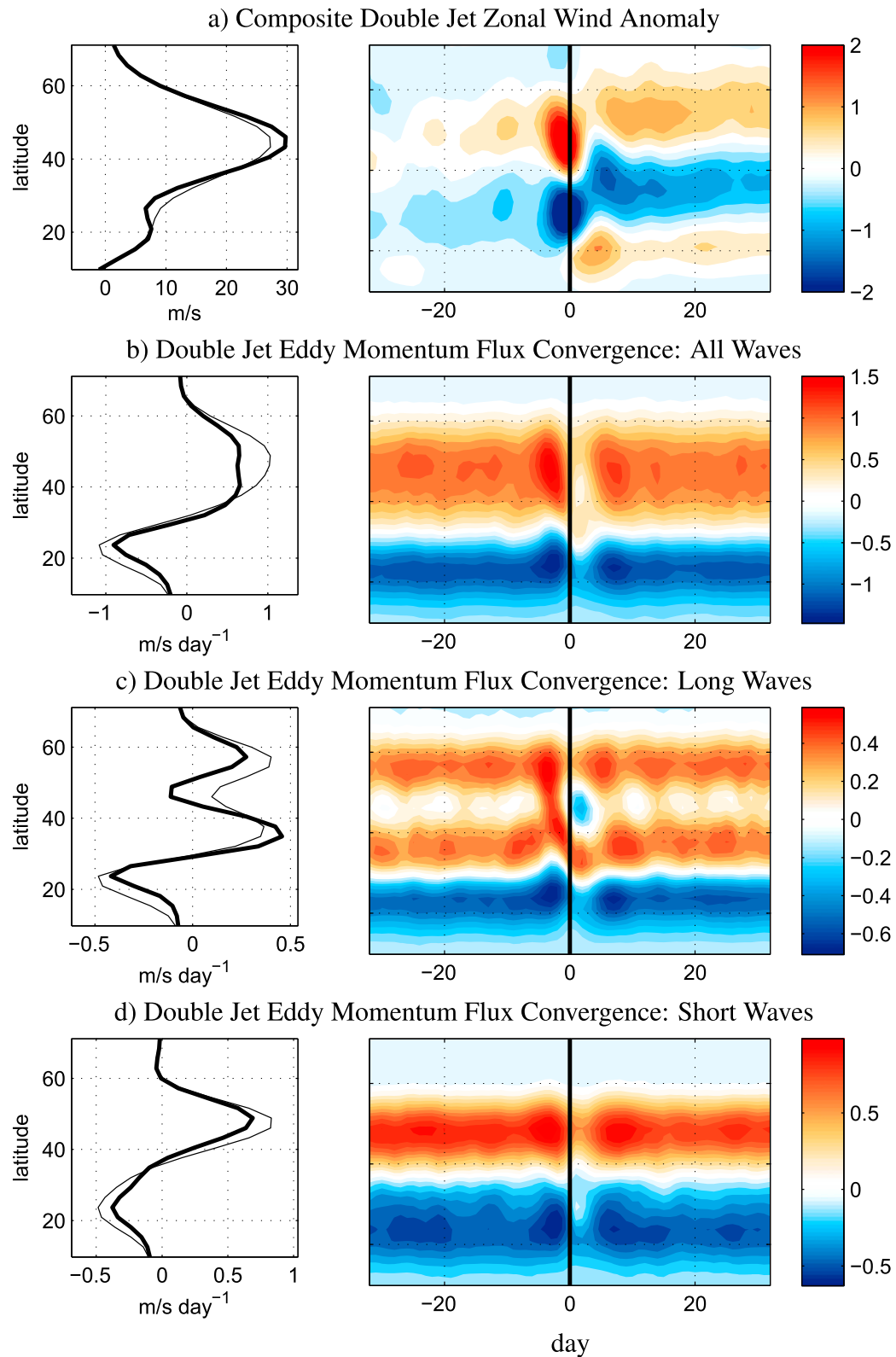


FIG. 12. (right) Composite of zonally averaged composite of (a) the zonal wind anomaly and the eddy momentum flux convergence for (b) all, (c) long, and (d) short waves as a function of days before and after the onset of a strong double-jet regime in experiment 2c. Eddy momentum flux convergence ( $\text{m s}^{-1} \text{ day}^{-1}$ ) is integrated vertically between 945 and 80 hPa. (left) The eddy momentum flux convergence at day 0 for each wave class for double-jet days (thick) and the all-time mean (thin).

strongly divergent in the days preceding and following day 0. Short waves are always convergent within the eddy-driven jet core and are overall weakened in the days following day 0.

The eddy-driven jet wind field shifts poleward, and an anomalous strengthening of the subtropical jet can be identified in the days following day 0 (Fig. 12a). This anomalous double-jet state persists beyond 20 days after the onset of the minimum interjet potential vorticity gradient at day 0.

This composite analysis of the vertically averaged zonal winds suggests that anomalous long-wave eddy momentum flux convergence within the eddy-driven jet and divergence within the interjet region assist in the strengthening and poleward shift of the eddy-driven jet. This strengthening enhances the horizontal wind shears within the interjet region and weakens the horizontal potential vorticity gradient until it reaches its weakly positive minimum value.

At day 0 and for the days following, the long-wave eddy momentum flux convergence abruptly changes sign within the eddy-driven jet region, and short-wave eddy activity is drastically reduced. Long waves now strongly accelerate the interjet region and weaken the eddy-driven jet core. Beyond +5 days, the eddy momentum flux fields return to average; however, the anomalous wind patterns generated from days 0 to +5 persist, suggesting a wave-driven shift in the equilibrium zonal wind state to that of a persistent, strong double jet.

## 7. Summary and conclusions

We created an array of single- and double-jet, steady-state, atmospheric regimes using an idealized, atmosphere-only spherical model described in section 2. These states are achieved by varying parameters controlling the strength of the stratospheric polar vortex and the degree of asymmetric heating between the hemispheres. Strong asymmetric heating and a strong stratospheric polar vortex lead to a double jet in the modeled Northern Hemisphere. These conditions also correspond to a strong wintertime hemisphere.

We focused on the effects of wave generation and breaking in the double-jet regime and found the patterns of eddy momentum flux convergence for long and short waves largely consistent with those of OV13, with notable differences in the importance of the interjet minimum phase speed bounds and the horizontal propagation of short waves. The atmospheric double jet, identified by a dual maximum in the upper-tropospheric zonal-mean zonal wind, features an interjet region identified by weakened potential vorticity gradients; however, this minimum is not strong enough to reflect

short waves as in the barotropic model. As seen in OV13, this interjet region can filter meridionally propagating waves by wavelength such that waves longer than the deformation radius may be propagated from the eddy-driven jet to the subtropical jet. OV13 found that this wavenumber-dependent filtering effect can be identified by minimum bounds on the zonal phase speed.

While minimum phase speed bounds and turning latitudes do not appear to have as strong a restriction to Rossby wave propagation as they did on the  $\beta$  plane of OV13, the separate effects of long and short waves on the eddy-driven and subtropical jets appear to be qualitatively similar. Short waves enhanced the eddy-driven jet, while long waves, active strongly in the double-jet case, acted as a negative feedback on the jet structure, leading to an acceleration of the interjet region and a merger of the jets.

Short-wave reflection was less apparent in this model than in that of OV13. Short Rossby waves were largely confined to the eddy-driven jet; however, short-wave eddy momentum flux divergence is evident in the subtropical jet (see Figs. 3c and 4c as examples), suggesting short waves were able to propagate through the interjet region and break at the core of the subtropical jet. The resulting eddy momentum flux from short waves breaking in the subtropical jet region leads to a tendency to accelerate the eddy-driven jet core and decelerate the subtropical jet. This interaction of short-wave eddy momentum flux divergence with the subtropical jet was not as evident in the  $\beta$ -plane model of OV13.

Long waves have a characteristic eddy momentum flux convergence pattern that differs greatly from short waves and classical theory for waves generated by baroclinic instability within the storm tracks. In a pressure-weighted, averaged, long-wave eddy momentum flux, convergence was associated with the interjet region and the poleward flank of the eddy-driven jet (Fig. 4); however, these features were predominately located in the lower half of the troposphere (Fig. 3b). We found these features are not an artifact of surface friction (Fig. 7).

The different pattern of eddy momentum flux convergence between long waves and short waves suggests different generation mechanisms for each wave class. By comparing a composite analysis of single- and double-jet days in section 6, we found that the long-wave eddy momentum flux convergence pattern leads to a deceleration of the eddy-driven jet core and an acceleration of the jet flanks. This pattern was most active in the double-jet regime, suggesting these long waves require the strong shear associated with a double jet. It is of future interest to determine the mechanism for generating long waves, particularly at wavenumber  $k = 5$ , in the double-jet configuration.

*Acknowledgments.* This material is based on work supported by the National Science Foundation under Grant AGS-1144302. The authors also wish to thank two anonymous reviewers for their extensive comments and helpful suggestions.

## APPENDIX

### Derivation of the Minimum Phase Speed Bounds

We will follow the derivation in Matsuno (1970) for the potential vorticity equation and refractive index, only we will allow for propagating Rossby waves by including the time-varying term. As in Matsuno (1970), we consider all quantities in terms of the log-pressure coordinate with a scale height of 10 km.

We follow the derivation for the refractive index of stationary waves in the upper troposphere given in Matsuno (1970); however, we also consider non-stationary waves. First, however, it should be noted that the derivation in Matsuno (1970) makes use of a modified version of the quasigeostrophic streamfunction  $\psi'$ , where  $\psi'$  is calculated with an ageostrophic modification to the meridional wind. Following Matsuno (1970), we approximate the perturbation meridional wind as

$$v' = \frac{1}{2\Omega a \sin\phi} \left( \frac{1}{\cos\phi} \frac{\partial\psi'}{\partial\lambda} - \frac{\bar{U}}{2\Omega a \sin\phi} \frac{\partial^2\psi'}{\partial\lambda\partial\phi} \right), \quad (\text{A1})$$

where the first term on the right-hand side of (A1) is the standard geostrophic balance term for the meridional wind and the second term is the so-called isoballic wind, a correction introduced by Matsuno (1970) to account for a spurious term in the energy equation. More information on this ageostrophic correction is discussed in Matsuno (1970) and in Andrews et al. (1987).

To obtain the refractive index for propagating Rossby waves on the stratified sphere, we start with the potential vorticity equation in terms of  $\psi'$  given in (9) of Matsuno (1970) and allow for time variation,

$$\begin{aligned} & \left( \frac{\partial}{\partial t} + \bar{U} \frac{\partial}{\partial\lambda} \right) \left[ \frac{\sin^2\phi}{\cos\phi} \frac{\partial}{\partial\phi} \left( \frac{\cos\phi}{\sin^2\phi} \frac{\partial\psi'}{\partial\phi} \right) \right. \\ & \quad \left. + \frac{1}{\cos^2\phi} \left( \frac{\partial^2\psi'}{\partial\lambda^2} \right) + \frac{f^2 a^2}{p} \frac{\partial}{\partial z} \left( \frac{p}{N^2} \frac{\partial\psi'}{\partial z} \right) \right] \\ & \quad + \frac{1}{\cos\phi} \frac{\partial\bar{q}}{\partial\phi} \frac{\partial\psi'}{\partial\lambda} = 0, \end{aligned} \quad (\text{A2})$$

where the mean meridional potential vorticity gradient has been introduced previously as (10).

Here,  $\bar{U} = \bar{u}(a \cos\phi)^{-1}$  is the time- and zonal-mean zonal angular velocity,  $\lambda$  is longitude,  $\phi$  is latitude,  $\Omega$  is

the rotation rate of Earth,  $f = 2\Omega \sin\phi$  is the Coriolis parameter,  $p$  is the pressure,  $N^2$  is the buoyancy frequency, and  $a$  is the radius of Earth.

We assume wavelike solutions to the streamfunction in the form of

$$\psi' = \sum_{k=1}^{\infty} \tilde{\psi}_m(\phi, z) e^{ik(\lambda - Ct)}, \quad (\text{A3})$$

where  $\tilde{\psi}$  is the amplitude of the perturbation streamfunction  $\psi'$ ,  $k$  is the zonal wavenumber,  $C = c(a \cos\phi)^{-1}$  is the angular phase speed, and  $c$  is the zonal phase speed.

By substituting these wavelike solutions for  $\psi'$  in time and longitude into (A2), we can obtain an expression for the amplitude of the wave in the meridional direction  $\tilde{\psi}$ :

$$\begin{aligned} & \frac{\sin^2\phi}{\cos\phi} \frac{\partial}{\partial\phi} \left( \frac{\cos\phi}{\sin^2\phi} \frac{\partial\tilde{\psi}}{\partial\phi} \right) + \frac{f^2 a^2}{p} \frac{\partial}{\partial z} \left( \frac{p}{N^2} \frac{\partial\tilde{\psi}}{\partial z} \right) \\ & \quad + \left[ \frac{(1/\cos\phi)(\partial\bar{q}/\partial\phi)}{\bar{U} - C} - \frac{k^2}{\cos^2\phi} \right] \tilde{\psi} = 0. \end{aligned} \quad (\text{A4})$$

It should be noted that, from here, Matsuno (1970) goes on to assume the amplitude of the wave solution  $\psi'$  can be further approximated by assuming it is proportional to  $e^{-z/2H_0}$ ; however, to do this, Matsuno (1970) assumes the atmosphere is isothermal. While this is not an accurate approximation for the troposphere, this approximation does provide a rough simplification to the minimum phase speed bound by introducing a concise term for the deformation radius. The isothermal approximation affects the term  $(f^2 a^2/p)(\partial/\partial z)[(p/N^2)(\partial\psi'/\partial z)]$  in (A4) and may be meaningful for vertically deep, large-scale waves that may feel more of a mean tropospheric temperature than a local temperature.

Equation (A4) may be considered a form of the Helmholtz equation in  $\phi$  and  $z$ , with the refractive index squared given by

$$\begin{aligned} n^2 = \frac{1}{\bar{U} - C} & \left[ 2(\Omega + \bar{U}) - \frac{\partial^2\bar{U}}{\partial\phi^2} + 3 \tan\phi \frac{\partial\bar{U}}{\partial\phi} \right. \\ & \left. - \frac{(af)^2}{p} \frac{\partial}{\partial z} \left( \frac{p}{N^2} \frac{\partial\bar{U}}{\partial z} \right) \right] - \frac{k^2}{\cos^2\phi}, \end{aligned} \quad (\text{A5})$$

where the potential vorticity gradient is as in (10).

For disturbances to take on a wavelike nature, this refractive index in (6) must be greater than zero. Likewise, the refractive index must be trivially less than  $+\infty$ . We can then convert these bounds to bounds on the angular phase speed:

$$\begin{aligned} \text{Nondivergent: } \bar{U}_{\min} &= \bar{U} - \frac{(1/\cos\phi)(\partial\bar{q}/\partial\phi)}{k^2/\cos^2\phi} \leq C \leq \bar{U} \\ \text{Isothermal approximation: } \bar{U}_{\min,d} &= \bar{U} - \frac{(1/\cos\phi)(\partial\bar{q}/\partial\phi)}{f^2/(NH_0)^2 + k^2/\cos^2\phi} \leq C \leq \bar{U}. \end{aligned} \quad (\text{A6})$$

In terms of the actual zonal wind velocity  $\bar{u}$  and the zonal phase speed  $c$ , these bounds are

$$\begin{aligned} \text{Nondivergent: } \bar{u}_{\min} &= \bar{u} - \frac{(1/a)(\partial\bar{q}/\partial\phi)}{k^2/(a^2 \cos^2\phi)} \leq c \leq \bar{u} \\ \text{Isothermal approximation: } \bar{u}_{\min,d} &= \bar{u} - \frac{(1/a)(\partial\bar{q}/\partial\phi)}{f^2/(NH_0)^2 + k^2/(a^2 \cos^2\phi)} \leq c \leq \bar{u}. \end{aligned} \quad (\text{A7})$$

#### REFERENCES

- Andrews, D. G., J. R. Holton, and C. B. Leovy, 1987: *Middle Atmosphere Dynamics*. International Geophysics Series, Vol. 40, Academic Press, 489 pp.
- Archer, C. L., and K. Caldeira, 2008: Historical trends in the jet streams. *Geophys. Res. Lett.*, **35**, L08803, doi:10.1029/2008GL033614.
- Bals-Elsholz, T. M., E. H. Atallah, L. F. Bosart, T. A. Wasula, M. J. Cempa, and A. R. Lupo, 2001: The wintertime Southern Hemisphere split jet: Structure, variability, and evolution. *J. Climate*, **14**, 4191–4215, doi:10.1175/1520-0442(2001)014<4191:TWSHSJ>2.0.CO;2.
- Barnes, E. A., and D. L. Hartmann, 2011: Rossby wave scales, propagation, and the variability of eddy-driven jets. *J. Atmos. Sci.*, **68**, 2893–2908, doi:10.1175/JAS-D-11-039.1.
- Bordi, I., K. Fraedrich, F. Lunkeit, and A. Sutera, 2007: Tropospheric double jets, meridional cells, and eddies: A case study and idealized simulations. *Mon. Wea. Rev.*, **135**, 3118–3133, doi:10.1175/MWR3464.1.
- Chan, C., and R. Plumb, 2009: The response to stratospheric forcing and its dependence on the state of the troposphere. *J. Atmos. Sci.*, **66**, 2107–2115, doi:10.1175/2009JAS2937.1.
- Chen, G., I. M. Held, and W. A. Robinson, 2007a: Phase speed spectra and the recent poleward shift of Southern Hemisphere surface westerlies. *Geophys. Res. Lett.*, **34**, L21805, doi:10.1029/2007GL031200.
- , —, and —, 2007b: Sensitivity of the latitude of the surface westerlies to surface friction. *J. Atmos. Sci.*, **64**, 2899–2915, doi:10.1175/JAS3995.1.
- COESA, 1979: *U.S. Standard Atmosphere, 1976*. NOAA, 227 pp. [Available online at <http://ntrs.nasa.gov/archive/nasa/casi.ntrs.nasa.gov/19770009539.pdf>.]
- Edmon, H. J., Jr., B. J. Hoskins, and M. E. McIntyre, 1980: Eliassen–Palm cross sections for the troposphere. *J. Atmos. Sci.*, **37**, 2600–2616, doi:10.1175/1520-0469(1980)037<2600:EPCSFT>2.0.CO;2.
- Eichelberger, S. J., and D. L. Hartmann, 2007: Zonal jet structure and the leading mode of variability. *J. Climate*, **20**, 5149–5163, doi:10.1175/JCLI4279.1.
- Eliassen, A. N., and E. Palm, 1960: On the transfer of energy in stationary mountain waves. *Geophys. Publ.*, **22** (3), 1–23.
- Gerber, E. P., and G. K. Vallis, 2007: Eddy–zonal flow interactions and the persistence of the zonal index. *J. Atmos. Sci.*, **64**, 3296–3311, doi:10.1175/JAS4006.1.
- , and —, 2009: On the zonal structure of the NAO and annular modes. *J. Atmos. Sci.*, **66**, 332–352, doi:10.1175/2008JAS2682.1.
- Hoskins, B., and T. Ambrizzi, 1993: Rossby wave propagation on a realistic longitudinally varying flow. *J. Atmos. Sci.*, **50**, 1661–1671, doi:10.1175/1520-0469(1993)050<1661:RWPOAR>2.0.CO;2.
- Kim, H.-k., and S. Lee, 2004: The wave–zonal mean flow interaction in the Southern Hemisphere. *J. Atmos. Sci.*, **61**, 1055–1067, doi:10.1175/1520-0469(2004)061<1055:TWMFII>2.0.CO;2.
- Kushner, P. J., and L. M. Polvani, 2004: Stratosphere–troposphere coupling in a relatively simple AGCM: The role of eddies. *J. Climate*, **17**, 629–639, doi:10.1175/1520-0442(2004)017<0629:SCIARS>2.0.CO;2.
- Lee, S., and H.-K. Kim, 2003: The dynamical relationship between subtropical and eddy-driven jets. *J. Atmos. Sci.*, **60**, 1490–1503, doi:10.1175/1520-0469(2003)060<1490:TDRBSA>2.0.CO;2.
- Matsumo, T., 1970: Vertical propagation of stationary planetary waves in the winter Northern Hemisphere. *J. Atmos. Sci.*, **27**, 871–883, doi:10.1175/1520-0469(1970)027<0871:VPOSPW>2.0.CO;2.
- Monahan, A., and J. Fyfe, 2008: On annular modes and zonal jets. *J. Climate*, **21**, 1963–1978, doi:10.1175/2007JCLI1841.1.
- O'Rourke, A. K., and G. K. Vallis, 2013: Jet interaction and the influence of a minimum phase speed bound on the propagation of eddies. *J. Atmos. Sci.*, **70**, 2614–2628, doi:10.1175/JAS-D-12-0303.1.
- Polvani, L. M., and P. J. Kushner, 2002: Tropospheric response to stratospheric perturbations in a relatively simple general circulation model. *Geophys. Res. Lett.*, **29**, 1181–1184, doi:10.1029/2001GL014284.
- Randel, W. J., and I. M. Held, 1991: Phase speed spectra of transient eddy fluxes and critical layer absorption. *J. Atmos. Sci.*, **48**, 688–697, doi:10.1175/1520-0469(1991)048<0688:PSSOTE>2.0.CO;2.
- Son, S., and S. Lee, 2005: The response of westerly jets to thermal driving in a primitive equation model. *J. Atmos. Sci.*, **62**, 3741–3757, doi:10.1175/JAS3571.1.
- Vallis, G., 2006: *Atmospheric and Oceanic Fluid Dynamics*. Cambridge University Press, 745 pp.
- , and E. Gerber, 2008: Local and hemispheric dynamics of the North Atlantic Oscillation, annular patterns and the zonal index. *Dyn. Atmos. Oceans*, **44**, 184–212, doi:10.1016/j.dynatmoce.2007.04.003.
- , —, P. Kushner, and B. Cash, 2004: A mechanism and simple dynamical model of the North Atlantic Oscillation and annular modes. *J. Atmos. Sci.*, **61**, 264–280, doi:10.1175/1520-0469(2004)061<0264:AMASDM>2.0.CO;2.
- Williams, L. N., S. Lee, and S.-W. Son, 2007: Dynamics of the Southern Hemisphere spiral jet. *J. Atmos. Sci.*, **64**, 548–563, doi:10.1175/JAS3939.1.
- Woollings, T., A. Hannachi, and B. Hoskins, 2010: Variability of the North Atlantic eddy-driven jet stream. *Quart. J. Roy. Meteor. Soc.*, **136**, 856–868, doi:10.1002/qj.625.